Synthesis of Cu and Co Doped and Co-Doped ZnO Nanocomposites for Catalytic Reduction of Methylene Blue and 4-Nitrophenol

Haji Kedir
`

A Thesis Proposal Submitted to Department of Applied Chemistry
School of Applied Natural Science
Office of Post Graduate Studies

In Partial Fulfillment for the Degree of Master of Science in Applied Chemistry (Industrial Chemistry)
Adama Science and Technology University

July, 2023
Adama, Ethiopia

Synthesis of Cu and Co Doped and Co-Doped ZnO Nanocomposites for Catalytic Reduction of Methylene Blue and 4-Nitrophenol

Haji Kedir Gelgelu

Supervisors :Main Advisor: Dereje Tsegaye (Ph.D.)
Co-Advisor: Buzuayehu Abebe (Ph.D.)

Department of Applied Chemistry School of Applied Natural Science
Adama Science and Technology University

July, 2023
Adama, Ethiopia

APPROVAL SHEET OF M.SC. THESIS
ADAMA SCIENCE AND TECHNOLOGY UNIVERSITY
SCHOOL OF APPLIED NATURAL SCIENCE
DEPARTMENT OF APPLIED CHEMISTRY
M.Sc. PROGRAM

We, the advisors of the thesis entitled "**Synthesis of Cu and Co Doped and Co-Doped ZnO Nanocomposites for Catalytic Reduction of Methylene Blue and 4-Nitrophenol**" and developed by Haji Kedir Gelgelu, hereby certify that the recommendation and suggestions made by the board of examiners are appropriately incorporated into the final version of the thesis.

Major Advisor	Signature	Date
Co-advisor	Signature	Date

We, the undersigned members of the Board of Examiners of the thesis by Haji Kedir Gelgelu, have read and evaluated the thesis entitled "**Synthesis of Cu and Co Doped and Co-Doped ZnO Nanocomposites for Catalytic Reduction of Methylene Blue and 4-Nitrophenol**" and examined the candidate during open defense. This is, therefore, to certify that the thesis is accepted for partial fulfillment of the requirement of the degree of Master of Science in Industrial Chemistry.

Chairperson	Signature	Date
Internal Examiner	Signature	Date
External Examiner	Signature	Date

Final approval and acceptance of the thesis is contingent upon submission of its final copy to the Office of Postgraduate Studies (OPGS) through the Department Graduate Council (DGC) and School Graduate Committee (SGC).

Department Head	Signature	Date
School Dean	Signature	Date
Office of Postgraduate Studies,	Dean Signature	Date

Declaration and Recommendation

Declaration

I hereby declare that this Master Thesis entitled "**Synthesis of Cu and Co Doped and Co-Doped ZnO Nanocomposites for Catalytic Reduction of Methylene Blue and 4-Nitrophenol**" is my original work. That is, it has not been submitted for the award of any academic degree, diploma or certificate in any other university. All sources of materials that are used for this thesis have been duly acknowledged through citation

_____	_____	_____
Name of the student	Signature	Date

Recommendation

We, the advisor(s) of this thesis, hereby certify that we have read the revised version of the thesis entitled "**Synthesis of Cu and Co Doped and Co-Doped ZnO Nanocomposites for Catalytic Reduction of Methylene Blue and 4-Nitrophenol**" prepared under my/our guidance by Haji Kedir Gelgelu submitted in partial fulfillment of the requirements for the degree of Master of Science in Industrial Chemistry. Therefore, we recommend the submission of revised version of the thesis to the department following the applicable procedures.

_____	_____	_____
Major Advisor	Signature	Date
_____	_____	_____
Co-advisor	Signature	Date

Acknowledgements

I, the researcher, would like to thank Dr. Dereje Tsegaye, my advisor, and Dr. Buzayew Abebe, my co-advisor, for their continuous, valuable, and exhaustive advice to accomplish the work. My gratitude also goes to Mr. Guta Amenu and Mr.Lemmi Bulto, analytical laboratory assistants, for providing technical support to perform laboratory activities for the synthesis of the nanocomposite; Mr. Leta, a SEM expert in the biology laboratory; Mr. Demeke, an XRD expert in the material engineering department; Alewubal Abebe, an FTIR expert at Bahir Dar University, for providing characterization facilities; and all other bodies who supported me to finalize my thesis.

Table of Contents

Table of Contents

List of Figures

List of Abbreviations and Acronyms

BNC	Binary nanocomposites
BV	Band valences
CB	Conduction band
CV	Conduction valence
DRS	Diffuse reflectance spectroscopy
EDS	Energy dispersive spectra
EDX	Energy dispersive X-ray
Eg	Energy bandgap
EXAFS	Extended X-Ray absorption fine structure spectroscopy
FTIR	Fourier transform infrared spectroscopy
MB	Methylene Blue
NC	Nanocomposites
NP	Nanoparticles
PL	Photoluminescence
ROS	Reactive oxygen species
SEM	Scanning electron microscope
TEM	Transmission electron microscopy
TNC	Ternary Nanocomposites
UV-Vis	Ultraviolet visible
XANES	X-Ray absorption near edge structure spectroscopy
XAS	X-Ray absorption spectroscopy
XRD	X-ray diffraction

Abstract

Large volumes of organic pollutants are produced today due to the rapid growth of urbanization and industries. Continuous electron-hole transfer and the ability of nanoscale materials to absorb visible light are critical for pollutant catalytic reduction. Cobalt and copper doped and co-doped ZnO nano composites were shaped by the sol-gel solution combustion (SG-SC) approach. The x-ray diffraction analysis confirmed the crystalline nature and interstitial doping of copper and cobalt in the zinc oxide lattice and the development of ZnO-CuO local contact. The PL and DRS-UV-vis investigations showed the NCs' superior charge transfer and considerable redshift (from 3.17 to 2.21 eV) properties over ZnO. TEM and SEM-EDS analyses confirmed the foam-type surface morphology, elemental composition, and dopant distribution. The NCs showed greater potency than ZnO NPs in the catalytic reduction reactions of 4-nitrophenol and methylene blue. Thus, the SG-SC approach has the potential for industrially scalable catalytic pollutant reduction applications.

Keywords: 4-nitrophenol, Catalysis, methylene blue, nanocomposite, porous

1. Introduction

Nowadays, the fast spread of urbanization and industries leads to the generation of huge amounts of organic pollutants. Toxic organic pollutants such as 4-nitrophenol (4NP) and thiazine methylene blue (TMB) contamination are worldwide problems (Godiya et al., 2023). 4-nitrophenol is highly stable and soluble in water and has mutagenic and carcinogenic effects on human health (Bagheri et al., 2022; Mejía and Reddy Bogireddy, 2022). A water-soluble thiazine methylene blue (TMB) dye is also toxic and has characteristic maximum wavelength peaks at 614, 663, and 292 nm due to the π to π^* electron transition (Naseer et al., 2022). Both toxic TMB and 4NP pollutants can be easily reduced in the presence of a reducing agent and an active catalyst (Basu et al., 2012). Currently, nanotechnology-based synthesis of nanoscale materials is an effective approach for treating and sensing toxic pollutants released into water bodies (Mejía and Reddy Bogireddy, 2022). Semiconductor nanomaterials such as ZnO are promising materials for several applications due to their noble optoelectrical and unique catalytic features, although they have certain weaknesses such as a small surface area and photon-induced electron-hole recombination (Wang et al., 2022). Doping transition metal elements such as copper, cobalt, and iron and forming a local contact with narrow bandgap metal oxides, such as CuO, are unique strategies for improving the above-mentioned ZnO drawbacks (Paraguay-Delgado et al., 2022). The radii of the cobalt (Co^{+2}, 0.072 nm) and copper ions (Cu^{+2}, 0.073 nm) are closer to that of the zinc ion (Zn^{+2}, 0.074 nm), which may not have a significant effect on the structural distortion during inclusion in the ZnO host (Shunmuga Sundaram et al., 2020). Cobalt (II) has a nearly identical radius to Zn, allowing for its high solubility in the ZnO lattice. Thus, doping of cobalt in the ZnO lattice makes a unique combination and forms nanocomposites (NCs) with a single phase, similar to bare ZnO (Fan et al., 2021; Kazmi et al., 2021). Copper oxide is a material with a high surface-to-volume ratio, tunable optical properties, and a narrow bandgap (1.2-2 eV) p-type metal oxide that is efficiently doped and forms a type II heterojunction with ZnO, resulting in effective charge transfer properties (Costas et al., 2022; Paraguay-Delgado et al., 2022).

The solution combustion reaction is an exothermic redox reaction in which the surfactants or fuel that act as reducers are oxidized and the precursor that acts as an

oxidizer is reduced during combustion to produce highly pure metal or metal oxide materials. The sol-gel solution combustion (SG-SC) synthesis, a combination of gelation and combustion processes, is one of the modifications of the solution combustion synthesis approach, which is used for synthesizing highly pure alloys, metals, and composites in addition to metal oxides (Mukasyan et al., 2015). The sol-gel solution combustion (SG-SC) approach is versatile for synthesizing highly efficient NCs materials for a wide range of applications (Deganello and Tyagi, 2018). It is a time- and energy-efficient approach in which self-initiated energy converts precursors into metal oxides without the use of external energy and within a very short time (Li et al., 2015). The final product produced during combustion is highly dependent on the type of surfactant or fuel used, the precursors used, and their ratio. The metal nitrate precursor that has an oxidant-type counter anion group has good solubility, oxidizing power, and a low decomposition temperature. During combustion, gaseous byproducts are removed instantly, making the material's surface more porous (Carlos et al., 2020).

Several reports on copper-doped ZnO and cobalt-doped ZnO NCs have been recently published using different methods. Chithira and his group proved the absence of independent peaks for cobalt metal or cobalt oxide on the XRD pattern analysis up to 10% cobalt doping. The non-occurrence of an independent peak was attributed to below-solubility-level substitution (Chithira and Theresa John, 2020). Kazmi et al. used a simple hydrothermal method to create cobalt-doped ZnO 1D nanowires without observing any independent peaks. Herein, it was reported that due to the close ionic radii between zinc and cobalt and the fact that the four-coordinate peak of the cobalt ion has a zinc substitution character, no ZnO crystal distortion was observed (Kazmi et al., 2021). The extrinsic doping of cobalt in the zinc oxide lattice without creating any Wurtzite structure distortion was also reported in different works (Borah et al., 2019; de Godoy et al., 2021). However, unlike cobalt, copper doping results in the formation of independent copper oxide peaks at lower copper amounts. For example, the copper-doped ZnO study conducted by (Morales-Mendoza and Paraguay-Delgado, 2021) and (Mahmoud et al., 2021) showed the formation of copper-independent peaks above 6% and 4% copper amounts, respectively. Here in these studies, the doping of copper up to the indicated percentage was confirmed based on the peak shift compared to the bare

ZnO. It was also reported that heterojunction formation between metal oxides improves charge transfer and visible light absorption properties.

However, according to the authors' search, there are only rare reports of the synthesis of these doped NCs by the SG-SC, and no reports on the use of the SG-SC to synthesize cobalt and copper co-doped ZnO with copper oxide heterojunction (Co, Cu, co-ZnO/CuO) NCs have been found. Thus, this study is aimed at synthesizing porous foam-type morphologies of binary cobalt-ZnO NCs (BNCs) and ternary Co, Cu, co-ZnO/CuO NCs (TNCs) using the SG-SC synthesis approach. The BNCs were synthesized for comparative purposes. The materials' porosity, composition, and dopant distribution were evidenced by the SEM-EDS/TEM analysis. The crystal structural analysis, the doping, and the formation of local contact were verified from the XRD pattern results. The source of the low-angle shift on the XRD pattern for TNCs was verified to be due to the copper inclusion. The presence of good diffusion-type charge transfer and electron-hole recombination hindrance properties were verified by the CV and PL analyses, respectively. The DRS-UV-vis analysis confirmed the presence of considerable band gap redshift. For the 4-nitrophenol and methylene blue catalytic reductions, the potentials of synthesized ZnO nanoparticles (ZnO NPs) and TNCs were tested, which confirmed the presence of a higher potential for the TNCs compared to the single ZnO NPs. Thus, the SG-CS approach is an efficient method for synthesizing catalytically improved doped materials for wastewater treatment.

1.2. Statement of the problem

Rapid industrialization, population, growth, and technological race worldwide have brought adverse consequences on water resources and, as a result, affect human health. Toxic non-biodegradable dyes, organic pollutants, and pharmaceuticals are among the chief hazardous materials released into the water bodies from various sources. These hazardous contaminants drastically affect flora and fauna globally, leading to health deterioration and new biomedical challenges. Innovation of novel nanomaterials to degrade pollutants and protect the environment is the utmost priority of the present researchers.

1.3. Objectives of the study

1.3.1. General objective

The general objective of this study is to synthesize and characterize ZnO nanoparticles (NPs) and Cu, Co-doped, and co-doped ZnO nanocomposites (NCs) for catalytic reduction of pollutants.

1.3.2. Specific objectives

- To synthesize ZnO, CuO, and Co_3O_4 NPs
- To synthesize Cu and Co doped ZnO NCs
- To synthesize Cu and Co co-doped ZnO NCs
- To characterize synthesized ZnO NPs and doped ZnO NCs using different analytical techniques such as XRD, UV-vis, PL, FTIR, and SEM.
- To investigate catalytic reduction of methylene blue dye.
- To study catalytic reduction of 4-nitrophenol

1.4. Significance and Beneficiaries

The outcome of this research will be important in the quest of wastewater treatment. Industries, the government & regulatory bodies, the local and scientific community are beleived to be among the beneficiaries from the outcome of the study. It is also believed that the research outcome is going to add a new modified research direction to the scientific communities.

2. Literature Review

2.1. Copper doped ZnO nanocrystals

Zinc and copper have similar electronic configurations and comparable atomic radii, although different structures, which limits the stability of the doped copper from dissolution. Doping of copper into the ZnO host improves the optical, electrical, and the magnetic properties, which is not observed in isolated constituents. A higher bandgap semiconductor metal oxide such as zinc oxide, ZnO, has outstanding thermal, optical, and electrical properties. ZnO also has higher light spectrum absorption efficiency and lower production cost (Abebe et al., 2020). However, the number and exact position of the dopant should be achieved to prevent the clustering of dopant atoms that have a damaging effect (Rossell et al., 2012). The oxidation states of copper (Cu, Cu (I), or Cu (II)) in the ZnO matrix is contentious and seems to be dependent on various parameters such as dopant concentration, temperature, and type of synthesis approach (Liu et al., 2013; Pashchanka et al., 2011). The general host-dopant molecular precursor's decomposition and reaction process for nitrate precursor (as an example) were given in equation 1 for ZnO and equation 2 for copper doped ZnO. Where x is the doping amount and δ is the spillover valence of oxygen (Gupta et al., 2016).

$$9[Zn(NO_3)_2.6H_2O] + 10[NH_2CH_2COOH]\ (Fuel) \rightarrow 9ZnO + 20CO_2 + 14N_2 + 79H_2O \quad (1)$$

$$xCu(NO_3)_2.3H_2O + (1 - x)Zn(NO_3)_2.6H_2O + Oxidant \rightarrow Cu_xZn_{(1-x)}O_{(2\ -\ \delta)} + \text{gaseous products} \quad (2)$$

The solution combustion process enables the final products of the nanomaterials with precise stoichiometric ratio, pronounced disparity, and uniform composition (Gao et al., 2016). Fig. 1 shows the solution combustion synthesis process accompanied by heating the fuel and oxidant to its ignition temperature. When a mixture of the metal nitrate precursors (which acts as oxidizer) and the urea fuel (as reducer) is heated to its ignition temperature, the metal ion-fuel complex starts to undergo combustion and form oxides. The combustion process is a self-propagation process, which could be controlled only by adjusting the ratio of reducing and oxidizing valances. Further calcination and reduction may help to stabilize the structure and reduce the metal as needed.

Gupta et al. synthesized highly porous doped materials by using a simple combustion approach in the presence of glycine as a fuel (Gupta et al., 2016). The combustion method is one of the methods that give pores/voids within the nanoparticles by releasing gas due to the exothermic reactions (Nagaveni et al., 2004). The fuel/reducer has a prominent role in facilitating the combustion process by creating an exothermic reaction and change in the morphology of the NPs. However, the porous materials synthesized by this approach exist in the disordered form, rather than the ordered which can be synthesized by choosing appropriate nanocrystal tethering and pore generating domain surfactants.

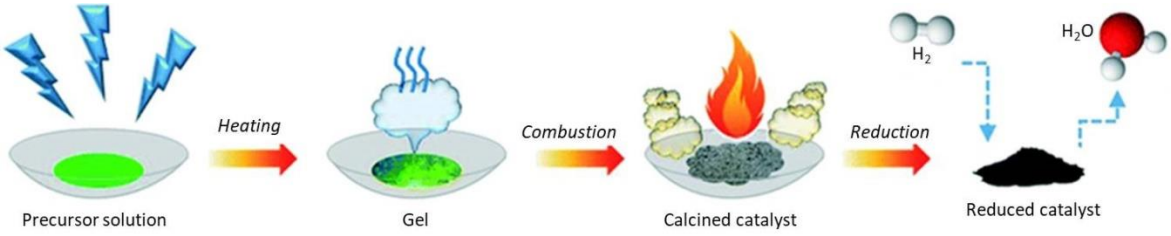

Figure 1. Schematic diagram of the synthesis process of catalysts by solution combustion approach (Gao et al., 2016).

Nowadays, several approaches such as sol−gel, Pechini, coprecipitation, solid-state reaction, hydrothermal, solvothermal, successive ionic layer adsorption and reaction, chemical bath deposition, plasma-enhanced chemical vapor deposition, spray pyrolysis, pulsed laser deposition, ball-milling, and sonochemical were employed for synthesizing the transition metal-doped ZnO materials (Singh et al., 2019). In the sol-gel and Pechini approach, the pH of the solution, aging, and annealing temperature are the major parameters affecting particle size, the nucleation and growth units, and morphology of the NMs (Alias et al., 2010). The coprecipitation technique is applied by drop-wise addition of the precipitating agent in the precursor solution, and calcinating the product at high temperature. The coprecipitation method is suitable for atomic-level mixing of the host and dopant at low temperature, however, it is difficult to control the nanocrystals (NCs) geometry (Singh et al., 2019). Both the solid-state reaction and coprecipitation technique present a decent stoichiometry of product, in which, the former needs high temperature than the latter. The solid-state reaction follows a homogeneous mixing of oxides and calcining at high temperatures. The synthesis of NMs by the hydrothermal and solvothermal techniques employs an autoclave with stepwise heating and cooling in the temperature range between 100 and 300 °C and keeping for several days. The

solvothermal method uses a different solvent rather than hydrothermal, which uses only water as a solvent. The spray pyrolysis and pulsed laser deposition methods are used to deposit thin films. Ball-milling is a simple process but needs high annealing temperature and consumes more time (Lemine et al., 2019).

Various concentrations of Cu (II) ions doped ZnO films were synthesized by sputter chamber deposition techniques with the help of sapphire as substrates (Liu et al., 2013). From the XRD pattern, a contraction of lattice due to the smaller size of Cu(I) and Cu(II) compared to the Zn(II) ion was noticed. Increasing the dopant concentration showed decreasing the intensity and increasing the FWHM values, which corroborates the reduction of both the crystallite size and crystallinity of the composite. Similarly, the observed shift in peak position towards a higher 2θ value, decreasing peak intensity, and peak broadening were also reported in various works (Chang et al., 2016; Chomean et al., 2017; Liu et al., 2015; Mahmoud et al., 2021; Xu et al., 2009) and explained to be due to the contraction of the c lattice due to the doping of Cu atoms into the ZnO lattice. No impurity peak conforming copper was found, which indicates the absence of structural distortion in ZnO lattice, although the XRD technique is not sensitive to small doped particles, rather than the dominant one. The transmission electron microscopy (TEM) can directly observe the doped nanocrystal; however, it can't give the correct oxidation state. Based on the HTEM image analysis, Pashchanka et al. interpreted the effective doping of copper ions into the ZnO lattice (Pashchanka et al., 2011). The experimentally obtained lattice fringe for Cu-doped ZnO (0.254 nm) is smaller compared to the normal ZnO interplanar spacing (Thakur and Mandal, 2021), which confirms the substitution of copper ion (which has ionic radii of 0.057 nm) with zinc ions (which has ionic radii of 0.060 nm).

An element-specific sensitive technique such as XAS (containing XANES and EXAFS) reveals the detailed information about the dopant oxidation state. Hu et al., reported that the XAS technique can be effectively used to study the local order, electronic environment, position, and distribution of doped copper (Liu et al., 2013). As indicated, the edge change is due to the incorporation of Cu at the Zn site, which causes minor disorder but does not affect the ZnO structure. From the background-subtracted and normalized Cu K edge XANES spectra; the detected pre-edge peaks, ca. 8977.5 eV and 8981 eV show for Cu (II) and trace amount of Cu (I) oxidation state, respectively. Related

XAS interpretation was also given on the bullet-like morphologies of Cu doped ZnO crystal synthesized by the sol-gel route (Bhardwaj et al., 2020). The shoulder at 9000.5 eV in all the doped films is due to the substitution of Cu in the Zn lattice. Also, the likenesses of the oscillations and magnitude of the Zn K-edge k^3-weighted EXAFS spectra for both bare ZnO and doped films show the substitution of Zn by Cu without distortion. The similarities between Zn and Cu K-edge in EXAFS analysis show the development of ZnO-like wurtzite structure around the Cu atom with Cu(II) oxidation state.

By using neutral beam sputtering techniques to create copper-doped ZnO, (Agarwal et al., 2019) showed that there was no structural distortion at low dopant concentrations. synthesized copper doped ZnO by neutral beam sputtering techniques and reported the absence of any structural distortion at low dopant concentration. However, increasing the dopant concentration results in the development of the copper peaks on the XRD pattern. From the optical properties obtained by UV-Vis spectral analysis, the bandgap energy of Cu-doped ZnO (15 %) was obtained to be smaller (2.8 eV) than ZnO bandgap energy (3.4 eV). This is probably due to the interband transition within the Zn 4s and Cu 3d band. As well interpreted on the surface plasmon resonance analysis, at a lower concentration, the doped material reveals the host behavior. Increasing above the optimum value the material can exhibit dual behavior. With the help of XANES spectra, the substitution of an empty ZnO *d* states by Cu(II) with trace amounts of Cu (I) was confirmed. A consistent XAS based XANES Cu(I) substitution result was interpreted in other work (Liu et al., 2015). In addition to XANES, the substitution of cuprous state (Cu(I)) in ZnO lattice was confirmed by XPS analysis (Xu and Shen, 2012). The sealed microspheres/semispherical shell morphology of the Cu doped ZnO composite was synthesized by chemical vapor deposition techniques.

In addition to XAS, the XPS analysis was also used to understand the doped copper oxidation states (Ali et al., 2019). Herein, the Cu doped ZnO material was synthesized by radio frequency magnetron sputtering technique from ZnO and CuO powders. The XPS analysis revealed the presence of both Cu(II) and Cu(I) oxidation states with Cu(I) in the interstitial position. Besides, increasing the dopant concentration results in reducing the amount of Cu(II) oxidation state and rising the Cu(I) oxidation state. The ZnO and CuO powders were also used to synthesize Cu-doped ZnO films deposited by using pulsed laser deposition technique under an oxygen partial pressure of 10^{-3} and 10^{-5} torr (Luo et al.,

2017). The composition, chemical state, and oxidation states of doped copper were analyzed by XPS analysis. In the oxygen-deficient sample (10^{-3} torr partial pressure), the Cu(I) state is dominant, while Cu(II) state is in the oxygen-rich sample (10^{-5} torr partial pressure).

2.2. Bi-metallic/Co-doped ZnO

Precise position and distribution of dopant can create shallow defect levels in the host matrix and tune the properties of the materials towards a specific application. Recently, two kinds of elements doping into semiconductor lattice have attracted substantial interest, as it could result in unusual characteristics compared with one element doping (Subash et al., 2012). The p-type doping and n-type doping were found to be difficult for low VB maximum and high CB minimum energy, respectively (Zhang et al., 2016). Thus, concurrently integrating the n-type and p-type dopants can be a feasible solution for the aforementioned problems. Also, co-doping increases the activation rate, dopant solubility, and carrier mobility. The Cu-Bi codoped ZnO nanospheres were synthesized by sol-gel-assisted hydrothermal method (Cao et al., 2021). From the XRD pattern, doping of Bi and Cu separately showed lower angle and higher angle diffraction peak shift owing to the respective higher and small size, compared to Zn size. This is attributed to the expansion and contraction of ZnO lattice during Bi and Cu substitution, respectively. The high-resolution scan XPS analysis confirms, the Bi^{3+} to be the major dopant chemical state. Besides, the main peak for O 1s XPS spectrum of Cu-Bi codoped ZnO is divided into five different peaks. Among these five peaks, the peak obtained at the binding energy of 530.54 eV and 532.18 eV were fits with Cu–O and Bi–O, respectively. The photocatalytic activity of Cu-Bi codoped ZnO is greater than ZnO, which is ascribed to the bandgap reduction for codoped materials, compared to Cu-, Bi-doped ZnO, and bare ZnO.

Spherical Cu and Ag NPs anchored on the surface of the ZnO materials synthesized by the green method showed UV-Vis absorption spectra intensity reduction and greater photocatalytic activity (Manjari et al., 2020). This local heterojunction between Ag/Cu NPs and ZnO was further confirmed on XPS analysis. The optical properties adjustment attributed to the characteristics of Co^{+2} d-d transitions in the Fe-Co codoped ZnO were also clearly shown in Beltrán et al., study (Beltrán et al., 2013). The presence of Fe and Co resulted in more charge transfer, which improves the ferromagnetism properties. Improvement in the optical and ferromagnetism properties ascribed to the codoping (Co-

Mn codoped ZnO) was also reported in (Pragna et al., 2021). The Ni-Cu codoped ZnO spherical materials synthesized by wet hydrolysis approach were showed pronounced PL spectra intensity reduction than bare and Ni- and Cu-doped ZnO counterparts (Priya et al., 2021). The codoped material showed complete quenching of the UV emission and growth of broad two visible emission bands at 380 nm and 460 nm, which is attributed to the Ni- and Co dopant, indicating its ability to serve as UV photodetectors.

The use of codoped ZnO as a photodetector was also studied in depth by (GuruSampath Kumar et al., 2020). The hetero-structured ZnO/Ga-Ag codoped ZnO nanorod material was synthesized by the two-step process, sol-gel-assisted hydrothermal approach. A slight lower angle shift was observed on the XRD pattern of the codoped material, yet confusing to interpret the effect based on the ionic radii, because Ga(III) has smaller ionic radii (0.62 Å) than Zn(II) (0.74 Å) and Ag(I) has greater radii (1.02 Å) than zinc ion. The incorporation of bimetallic dopant showed a superior (nearly 20 times) PL emission intensity drop, which increases additional CB electrons and also reduces material bandgap. The fabricated codoped hetero-structured nanorod UV-photodetector showed two times photoresponse compared to bare ZnO at 13.5 mW/cm^2 UV power density.

In addition to the transition metal doping, nonmetal doping participate in the band narrowing and amends the materials property towards visible light absorption. Transition metal ion (Cu) as a p-type and non-metal ion (N) as n-type codoped ZnO porous material were synthesized by (Gupta et al., 2016) using the combustion and hydrothermal methods. The materials were synthesized by keeping the amount of N constant and increasing the amount of copper. From the XRD pattern analysis, increasing the amount of copper showed lattice contraction, attributed to the substitution of smaller Cu ionic radii with greater Zn ionic radii. In this study, the absorption of light in the visible region and bandgap lessening were seen for N-Cu codoped ZnO than Cu-, N-doped and bare ZnO. The incorporation of both Cu (Cu(I) and C(II)) and N in the ZnO lattice were also confirmed on the XPS analysis. Herein, the creation of a sub-energy level band below the host CB and above the VB was suggested due to the transition metal and nonmetal doping, respectively. The created sub-energy level acts as a photogenerated electron-hole sinker, thus prolonging the electron-hole recombination.

Besides, Ce-Ag codoped–ZnO material prepared by the solvothermal method also showed a superior surface area and optical property improvements (Subash et al., 2012). Compared to the bare ZnO, the codoped-ZnO material showed approximately five times less average crystallite size. The greater the surface area, the higher the sorption properties and enhances the photon-assisted degradation. The redshift on the optical spectra, occurred due to a new energy level, on the DRS spectra attributed to the existence of noble contact between the host and dopant (Ag–ZnO–Ce). Besides, the lower PL intensity for codoped compared to the bare ZnO also shows lessening of electron-hole recombination. The smaller the recombination the higher the Naphthol Blue Black dye degradation in aqueous solution under solar light irradiation. The photo-generated electron transfer from ZnO CB to both doped Ce and Ag metal was also reported on reducing the electron-hole recombination synergistically.

In addition to the magnetic and optical properties, the electrical properties of ZnO were also boosted by doping of Cu in ZnO lattice and further decorating it with different percentages of Ag (Ag@Cu-ZnO). Small peaks ascribed to Cu and Ag and higher angle shift owning to interstitial site impurity incorporation were detected on the XRD pattern. Increasing the average crystallite size with increasing Ag amount was attributed to the replacement of greater size Ag ion (1.26 Å) with smaller size Zn ion (0.74 Å). In this study, the incorporation of Cu into the ZnO lattice was understood from the FTIR band shift.

2.3. Solution combustion synthesis

The LaMer model gives insight into the overall process of the nanocrystal formation starting from the precursor decomposition. However, in addition to the reduction, growth, and nanocrystal formation process, the development of complexes between the precursor’s anions and fuels/surfactants/solvents, which result in the combustion process once the ignition temperature is reached, should also be critical within this document. The nanocrystal probably contains complexes formed between the precursor's anions and surfactants/fuels. Further dehydration and heating to ignition temperature results in combustion, commonly known as solution combustion synthesis (SCS). SCS is a complex self-sustained exothermic reaction process, initiated between the surfactants or/and organic fuel and metal nitrates. The SCS follows (i) a molecular level mixing to form the colloidal NPs

(sol), (ii) evaporating the water molecules to form a gel, (iii) creating a high locally initiated reaction temperature, which is activated by low preheating temperature (Novitskaya et al., 2021), (iv) the combustion front spreads along the rest of the media, and (v) finally, diminishing of the temperature of the overall system due to the quenching effect through the evolution of gases. The occurrence of gas evolution results in decreasing the combustion front velocity and temperature by blocking the crystal growth. This in turn increases the final product's total porosity/textural properties (González-Cortés and Imbert, 2013).

Fig. 2(a) shows the mechanism of microstructures synthesis (combustion wave capturing) under the controlled infrared (IR) measurement. The *in-situ* high-speed IR camera uses to control the combustion wave and measure the width of the combustion wave (Xanthopoulou et al., 2018). Herein, two cases may exist; the first case is a reaction of the gaseous products during the nitrate decomposition, in which combustion starts from many points and results in the formation of spongy/foam-like structure of metal oxides (Fig. 2(b)). In the second case, the reaction may start at one spot/point, through which the bright reaction front starts to propagate in one direction and form a long wire metal oxide (Carlos et al., 2020) (Fig. 2(c)). Finally, the primarily developed metal oxide may react with the reducing gases/atmosphere (H_2 and NH_3, produced during gas-phase combustion) or/and with oxygen in the atmosphere resulting in reduction of metal oxides to zerovalent metal (Nersisyan et al., 2017). Following the SCS procedures, the combusted materials may be further calcined at high temperatures to decompose the un-burnt impurities and improve the crystallinity of the materials (Gao et al., 2016). Of course, increasing the furnace temperature may facilitate the detonation time and crystallinity, although it increases the crystallite sizes of the material. The increasing crystallite size increase/agglomeration process with increasing temperature is due to the melting of the particles and fussing into a larger aggregate, commonly known as melt-induced aggregation. The aggregation mechanism is by diffusion of surface matter (such as ash, which melts and facilitates the adhesion process) around the particles resulting in the assembly (Morris et al., 2018).

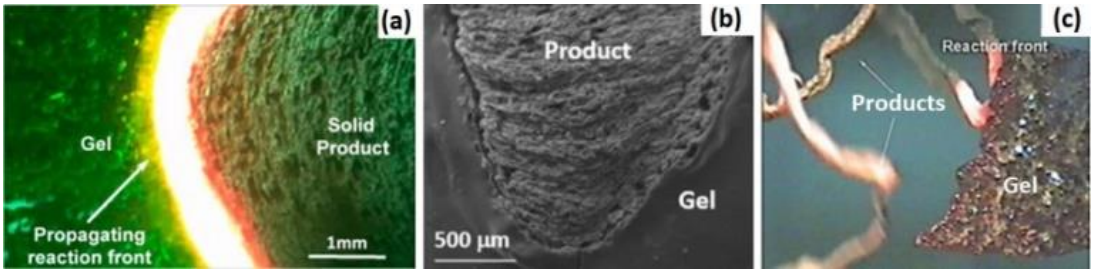

Figure 2. Scheme representation of the self-sustained combustion process: (a) Infrared images for reaction front propagation (b) SEM images of quenched front in a nickel nitrate-glycine gel (Xanthopoulou et al., 2018) and (c) iron nitrate-glycine (Nersisyan et al., 2017).

SCS creates a pure metal oxide material with very high stability and a good surface area within a short reaction time (Cai et al., 2020). This approach-based synthesis of semiconductor metal oxide materials is time-/energy-efficient and creates a well-defined porosity due to the evolution of gases (Ajamein and Haghighi, 2016). The porosity in the materials assists in the interfacial mass-/ion transport, especially in sorption, energy storage, catalysis, and sensing applications (Li et al., 2012; Ren et al., 2012). Besides, the technique is also simple, needs a low-cost instrument, and yields highly pure products. It neglects the time consumed by the purification or the post-synthesis treatment procedures compared to the other established approaches (Abu Hatab et al., 2022; Delfani et al., 2022). In this approach, once the mixture reaches the ignition temperature, self-generated energy raises the reaction temperature to 4000 ^{o}C (Rajeshwar and de Tacconi, 2009), and within seconds/minutes, the precursor is converted into the corresponding stable metal/metal oxides.

3. Materials and Methods

3.1. Chemicals and Reagents

Zinc nitrate, $Zn(NO_3)_2.6H_2O$,99.5%; PVA polymer, copper(II)nitrate trihydrate, $Cu(NO_3)_2.3H_2O$,99.5%; and cobalt (II) nitrate hexahydrate, $Co(NO_3)_2 . 6H_2O$, 98%; were used for the synthesis of nanoparticles (NPs) and nanocomposites.

3.2. Synthesis of ZnO NPs

Using previous reports as a starting point (Gao et al., 2016; Liu et al., 2016), the ZnO NPs, BNCs, and TNCs were synthesized by the SG-SC synthesis approach. In detail, the polyvinyl alcohol (PVA, MW: 85,000–124,000) was dissolved in hot distilled water (heated to approximately 70–80 °C) for about 25 minutes and cooled to room temperature. The zinc nitrate precursor ($Zn (NO_3)_2.6H_2O$, 99.5%) was dissolved in this cooled PVA polymer to form a 0.25-M solution concentration. The PVA-precursor complex sol solution (Zhang et al., 2012) then dried at about 80 to 110 °C within 2–3 hours. The obtained PVA-precursor complex gel was then combusted by increasing the temperature further to 150–250 °C within 5–10 minutes. Finally, the combusted byproduct was crumpled slowly and annealed at 500 °C for three hours. 500 °C is the calcination temperature optimized using the TGA-DTA technique. The synthesized materials were then kept for further analysis and application tests.

3.3. Doping and co-doping of ZnO NPs

The host zinc precursor was mixed with appropriate amounts of copper (II) nitrate trihydrate ($Cu(NO_3)_2.3H_2O$, 99.5%) and cobalt (II) nitrate hexahydrate ($Co(NO_3)_2. 6H_2O$, 98%) dopant precursors to make the BNCs and TNCs. The synthesized TNCs were coded as TNCs1, TNCs10, and TNCs20. TNCs1 represents 0.5% for each copper and cobalt dopant salt precursor (which is 1%), and 99% for the host zinc precursor. Similarly, TNCs 10 and 20 represent 5% and 10% of each dopant salt, respectively. For synthesized BNCs, BNCs1 and BNCs20 represent 1 and 20% cobalt and copper, respectively.

3.4. Characterization

PVA-ZnO thermal stability was studied by the TGA-DTA techniques (Shimadzu DTG60H). The crystal structure, approximate crystallite size, and crystallinity were understood from the X-ray diffraction technique (XRD-7000, Shimadzu) with Cu Kα radiation (at an x-ray radiation wavelength of 0.15406 nm, a current of 30 mA, and a

voltage of 40 kV). Materials optical properties were studied using the DRS-UV-vis (Shimadzu, UV-2600) and PL (PL, Agilent, CaryEclipse fluorescence spectrophotometer (MY18490002) with a 600 nm/min scan rate) analyses at a laser excitation wavelength of 325 nm). FTIR spectroscopy was used for chemical bonding analysis. Materials' electrochemical property measurements were done by the CV instrument (CV, CH electrochemical analyzer instrument (CH 660E potentiostat) in the three-electrode system, in which the NPs and TNCs-modified glassy carbon electrodes were used as the working electrodes, platinum wire as a counter, and Ag/AgCl as a reference electrode. The SEM (JCM-6000Plus) and TEM (JEOL TEM 2100 HRTEM) techniques were used for morphological, particle size, and material crystallinity analyses.

3.5. Catalytic activity

To test the reduction potential of ZnO NPs and TNCs, the synthetic pollutants 4-nitrophenol and methylene blue were used. According to a recent report (Ali et al., 2022), with a slight concentration change, the ability of synthesized NPs and TNCs to catalyze the reduction of 4-nitrophenol to 4-aminophenol was tested. The experiment began with the preparation of a 0.01 M 4-nitrophenol stock solution, which was then diluted to a concentration of 0.11 mM. A 0.05M sodium boron tetra hydride, $NaBH_4$, was added as a reducing agent to the above-mentioned dilute 4-nitrophenol solution. The catalyst (NPs and TNCs, 10 mg) was then added to the $NaBH_4$ and 4-nitrophenol mixture solution. The catalytic reduction process was controlled using the ultraviolet-visible instrument immediately after the addition of the catalyst.

Sodium borohydride ($NaBH_4$) was also used as a reducing agent to investigate methylene blue reduction reactions (Naseer et al., 2022). In detail, the 1000 ppm stock solution of TMB was prepared and further diluted to 15 ppm as a synthetic pollutant. The excess $NaBH_4$ (45 mg) was then dissolved in a 30 mL solution of a synthetic pollutant containing 15 ppm TMB. Then, after 2–3 minutes, 10 mg of ZnO NPs as well as NCs were added to the above TMB and $NaBH_4$ mixture. The reduction reaction was then controlled using ultraviolet-visible spectroscopic techniques (UV-vis, P9 double-beam spectrophotometer).

4. Results and Discussion

4.1. Characterizations

4.1.1. Thermogravimetric-differential thermal analysis

The thermal stability and degradation behavior of the polymer (PVA) and zinc nitrate precursor, which were used for selecting an optimum heat treatment, were studied by the thermogravimetric-differential thermal analysis (TGA-DTA). The TGA-DTA analysis was carried out in a nitrogen atmosphere using the DTG analytical technique. The TGA is a technique used to measure the change in mass loss as a function of temperature. For PVA-ZnO decomposition, mainly three mass loss steps were observed, as shown in Fig. 3. The first two small and broad peaks are due to the dehydration of surface and/or crystallized (metal hydroxide decomposition) water and/or the amorphous parts of PVA decomposition. The third intense peak is due to the decomposition of the PVA main chain (Kumar et al., 2019; Rahmanian et al., 2015). The PVA-ZnO composites were stable within the range of 470–570 °C, which was then selected as the optimum calcination temperature used to decompose the PVA surfactant and other impurities that have a boiling point of less than 500 °C.

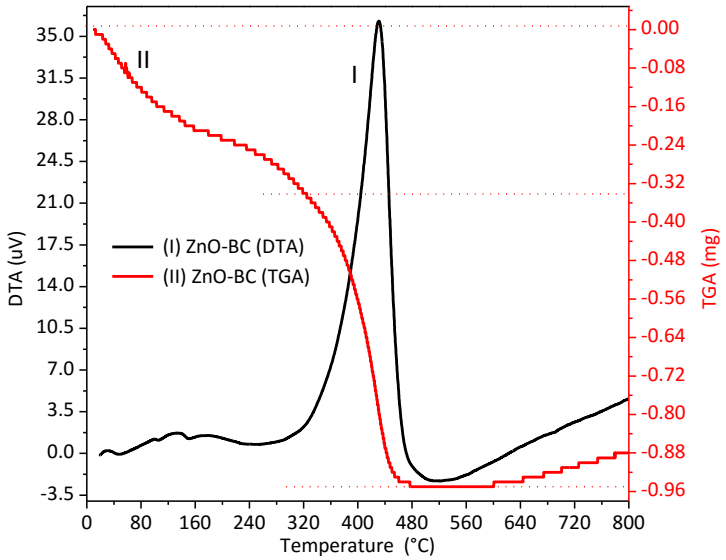

Figure 3. The TGA-DTA thermal stability analysis of PVA-ZnO NCs: BC represents before calcination.

4.1.2. X-ray diffraction analysis

The capping ability of PVA with various amounts, which is used to select the optimum PVA amount, was studied, as shown in Fig. 4. The diffraction patterns of dry powder NPs and TNCs powder were analysed, as shown in Fig. 5a–c. The XRD diffraction pattern of BNCs (Fig. 6a–f) was also given for comparison purposes. The XRD diffraction pattern gives information about dopant inclusion and heterojunction, the crystallite size, and the crystallinity of the synthesized materials. The diffraction pattern planes of ZnO NPs and 1% TNCs matched with the wurtzite ZnO structure, according to the standard reflection pattern result (JCPDS 00-036-1451; Fig. 5a and 5b). Increasing the dopant percentage to 10% and 20%, however, results in the appearance of independent copper peaks, primarily at 2θ values of 38.7 and 35.5 degrees. However, the cobalt-independent peak was not detected up to 20% (10% copper and 10% cobalt) dopant inclusion for the TNCs, indicating that the solubility is still below the solubility level (Chithira and Theresa John, 2020).

To check the solubility level of cobalt dopant in the zinc oxide host, 20% cobalt dopant was used as the dopant percentage, as shown in Fig. 6a-c. An independent peak was observed in the 20% dopant amount, primarily at 2θ values of 36.8^{o}. Besides, on the BNCs' XRD pattern, no peak shift was observed (Fig. 6c); however, on the TNCs, there is a visible low-angle shift relative to a single ZnO (Fig. 5c), confirming that the shift is due to the copper inclusion. The XRD pattern peak for 20% copper dopant was also depicted in Fig. 6d-f. Increasing the amount of copper to 20% resulted in the development of two additional monoclinic phases of CuO peaks at 2θ values of 35.5^{o} and 39^{o} with the corresponding planes of (002, 11-1) and (200, 111), respectively (Costas et al., 2022; Paraguay-Delgado et al., 2022). The slight low-angle shift for doped NCs compared to single ZnO NPs confirms the inclusion of copper in the ZnO lattice. Thus, on the 20% doped NCs, both doping and heterojunction took place. The formation of doping and p-n type II heterojunction is important in the photogenerated electron-hole separation (charge transfer) process, which improves the material's photo response properties (Costas et al., 2022). The development of an independent CuO phase above the optimum dopant percentage (solubility level) was also reported in recent works (Paraguay-Delgado et al., 2022).

The diffraction peak for single CuO and Co_3O_4 was also given, and their diffraction pattern planes also matched with the monoclinic (JCPDS 00-048-1548) (Costas et al., 2022) and fcc (JCPDS, File No. 00-042-1467) structures, respectively (Thangasamy et al., 2017). Cobalt doping in the ZnO lattice induces a mid-interband state near the ZnO conduction band, resulting in an increase in visible light absorption (Chen et al., 2021).

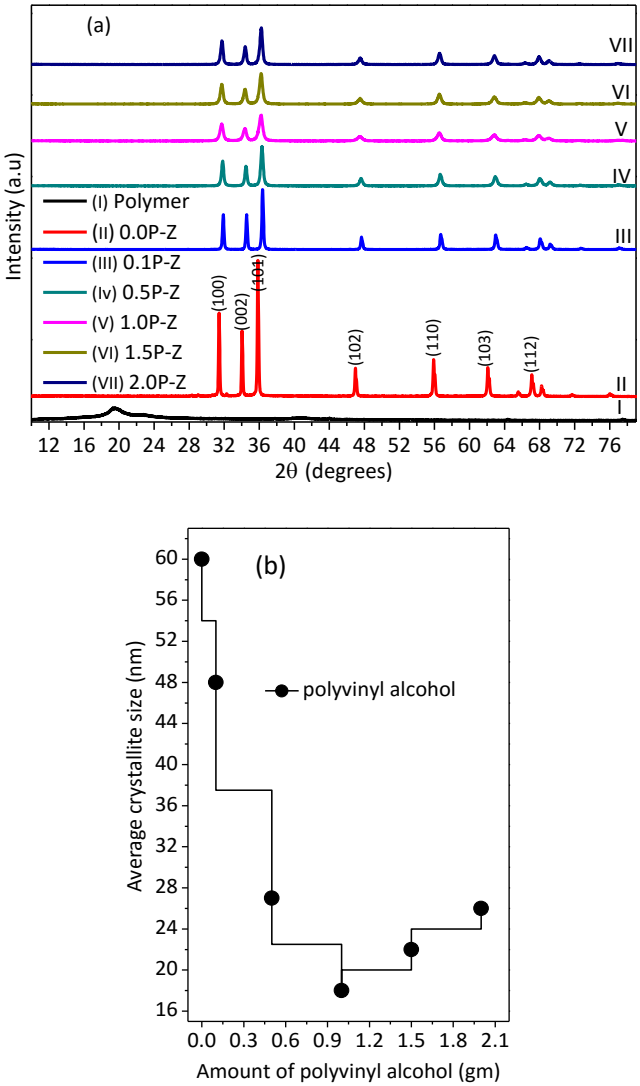

Figure 4. PVA amount optimization using the XRD pattern: (a) The XRD pattern of raw PVA and ZnO NPs synthesized by taking different amounts of polyvinyl alcohol (0.0–2.0 g). (b) The average crystallite size versus the amount of polyvinyl alcohol plot for ZnO NPs synthesized using different amounts of polyvinyl alcohol.

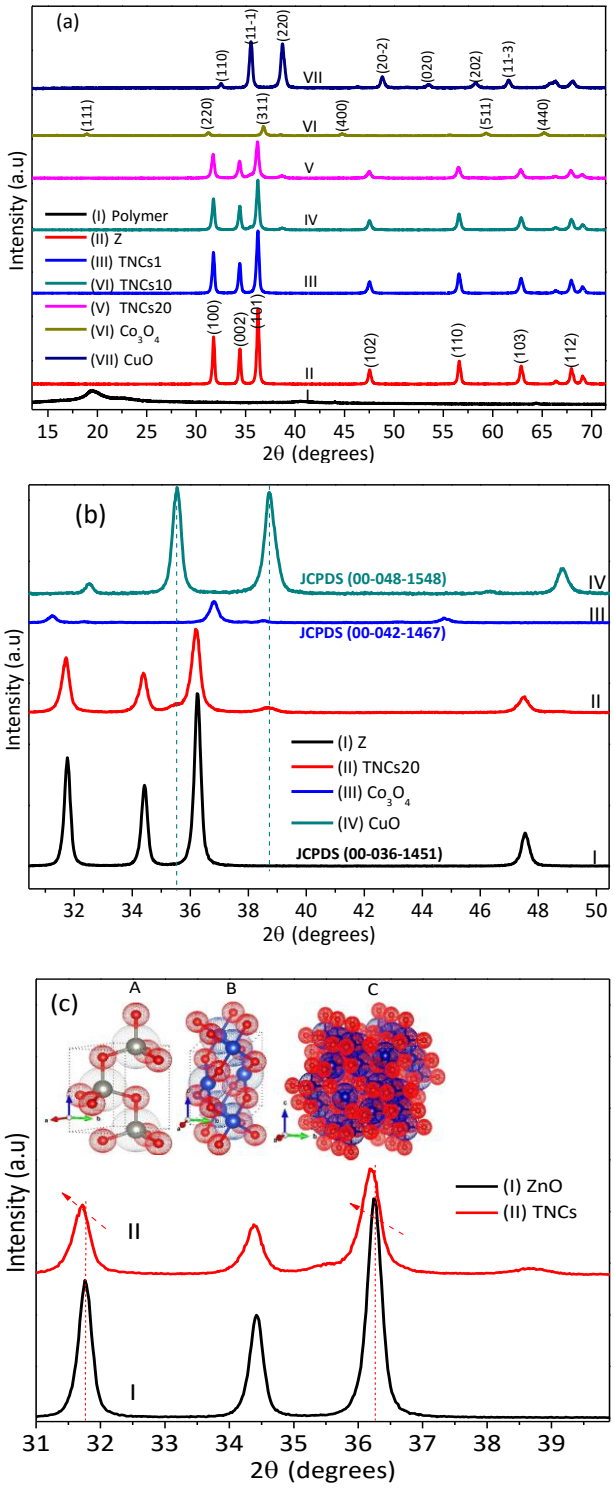

Figure 5. The XRD diffractogram analysis for NPs and TNCs: (a) XRD patterns of polyvinyl alcohol, zinc oxide, copper oxide, and cobalt oxide NPs, as well as 1%, 10%, and 20% TNCs. (b) magnified XRD patterns of zinc oxide, copper oxide, and cobalt oxide NPs, as well as 20% TNCs. (c) magnified XRD patterns of ZnO NPs and 20% TNCs; the inset structures in Fig.5c are the CIF data from the AMCSD database and the VESTA software-based crystal structures of ZnO (A), CuO (B), and Co_3O_4 (c) NPs.

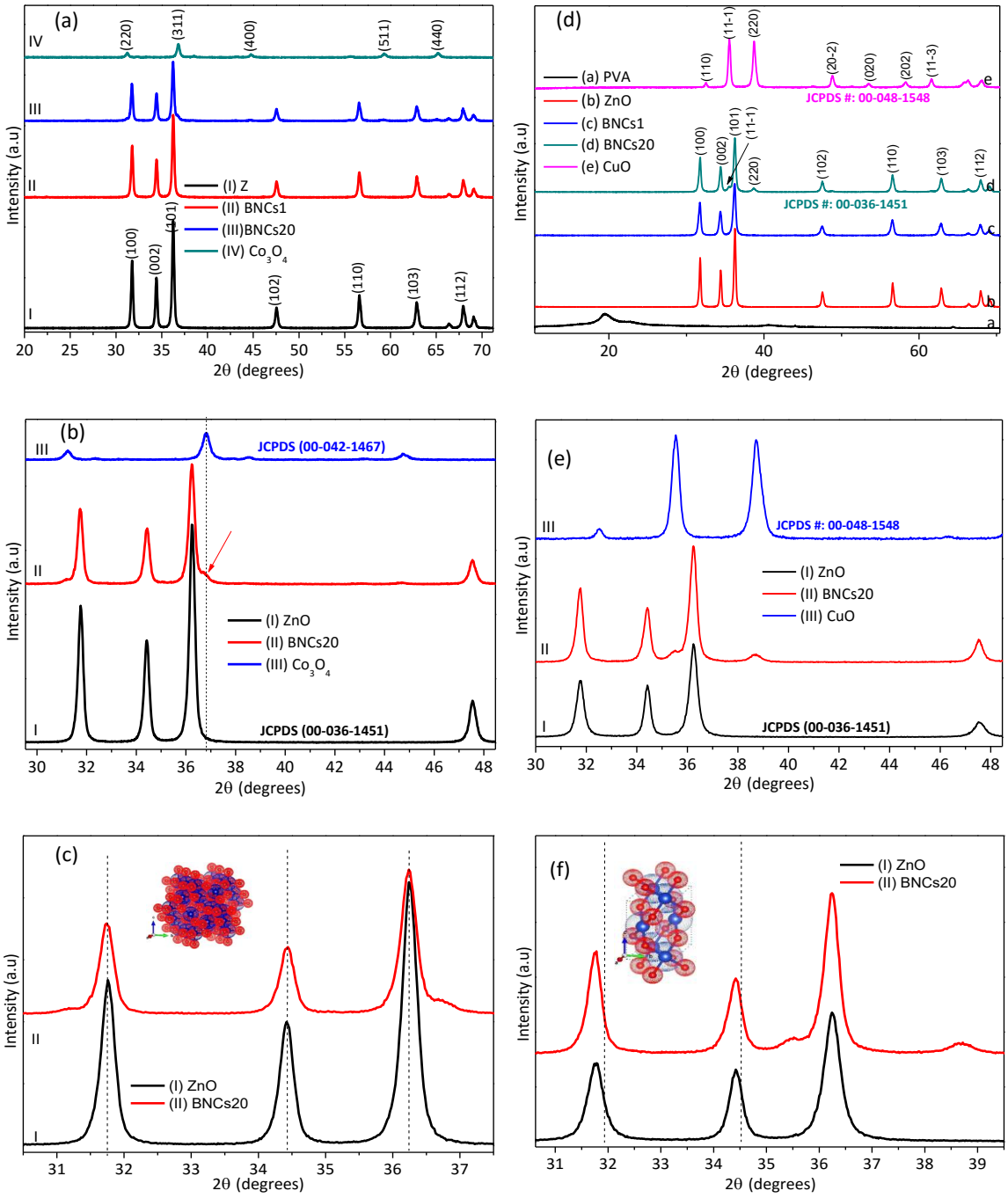

Figure 6. The XRD diffractogram analysis for nanoparticles and BNCs: (a) The XRD patterns of zinc oxide and cobalt oxide NPs and 1% and 20% BNCs. (b) The magnified XRD patterns of zinc oxide and cobalt oxide nanoparticles and 20% cobalt doped-BNCs. (c) The magnified XRD patterns of zinc oxide and 20% BNCs. (d) The XRD patterns of zinc oxide and copper oxide NPs and 1% and 20% BNCs. (e) The magnified XRD patterns of zinc oxide and copper nanoparticles and 20% copper doped-BNCs. (f) The magnified XRD patterns of zinc oxide and 20% BNCs.

The ionic radius of both cobalt ions (Co^{+2}, 0.072 nm) and copper ions (Cu^{+2}, 0.073 nm) is closer to that of the zinc ions (Zn^{+2}, 0.074 nm), which may not have a visible effect on the geometry of the ZnO host during inclusion (Mahmoud et al., 2021; Morales-Mendoza and Paraguay-Delgado, 2021; Shunmuga Sundaram et al., 2020). Recent work also reported (Chithira and Theresa John, 2020) the properties of cobalt substitution in the ZnO lattice up to 10% without inducing additional cobalt metal or cobalt oxide crystal. The absence of an independent crystal for cobalt up to 10% is due to the similar ionic radii between cobalt and zinc and the greater solubility level of cobalt (Kazmi et al., 2021). Even though copper has a similar size to Zn, its solubility and inclusion percentage in the ZnO lattice are less than cobalt's, resulting in the formation of an independent crystal for copper oxide after 5%, as shown in Fig. 6a. A similar independent monoclinic copper oxide formation above 5% is also reported in a recent study (Morales-Mendoza and Paraguay-Delgado, 2021). The crystal structures of ZnO (A), CuO (B), and Co_3O_4 (c) NPs (Fig. 6c inset) were developed using the VESTA structure visualization software based on the AMCSD-database CIF data.

4.1.3. Photoluminescence analysis

The optical properties of NCs and NPs are determined by photoluminescence spectroscopy, as shown in Fig. 7. In general, ultraviolet and visible emissions from ZnO can be attributed to near-band edge (NBE) emission and defect (deep level) emission. NBE, a characteristic of ZnO emission, is caused by free exciton recombination (Islah-u-din et al., 2020). Many studies have proposed that the presence of defect emission in ZnO assists excited electron transitions from the ZnO conduction band (CB) to defect states such as chemisorbed O_2 on the intermediate active sites ($ZnO(OH)_x$ and $ZnO(O_2)_y$) that occur during synthesis. (Ma et al., 2019). The defect emission for single ZnO NPs and 1% TNCs is not very visible in this study, compared to the 20% TNCs. TNCs showed a significant reduction in intensity and exhibited a completely new and intense defect emission peak in the visible region of 416 nm, which is attributed to violet emission occurring as electrons transferred from the shallow donor level to the ZnO valence band, most likely due to Cu or Co impurities (Islah-u-din et al., 2020).

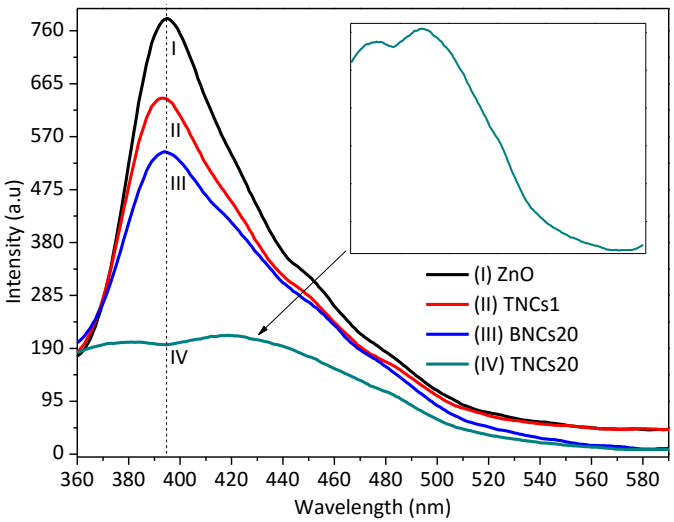

Figure 7. Photoluminescence spectra of ZnO NPs, BNCs, and TNCs. TNCs showed a significant reduction in intensity. In comparison to single ZnO, redshifts were observed in the TNCs.

Compared to the single ZnO, a considerable intensity reduction for 20% TNCs is also reported to be due to the change in the crystalline quality as a result of doping (Chithira and Theresa John, 2020). Besides, the TNCs also showed a greater intensity reduction compared to the BNCs, indicating the effect on the ternary is due to the combined effects of copper and cobalt dopants. Of course, this intensity reduction for TNCs shows the presence of great electron-hole recombination reduction properties, which have great effects on the mass production of an oxidizing agent such as the hydroxyl radical. Hydroxyl radicals play great roles in several fields. In addition, the single ZnO characteristic band edge emission at 395 nm showed a red shift towards 419 nm on the TNCs (see the magnified inset in Fig. 7).

4.1.4. Diffuse reflectance ultraviolet-visible analysis

Figure 8a shows the DRS-UV-vis-based optical properties analysis of ZnO and TNCs20. ZnO NPs showed greater reflection (starting from 370–440 nm) than the TNCs. The additional absorption band in the visible region for TNCs confirms doping level creation below the ZnO conduction band (Chithira and Theresa John, 2020). These additional bands and doping level creation assist a shallow level *d-d* electron transition, which hinders the photon-induced electron-hole recombination (Muthukumaran and Gopalakrishnan, 2012). The direct and indirect band gaps of

the materials were determined from the Kubelka-Munk relation by extrapolation of the linear region towards the x-axis, as shown in Fig. 8b and 8c.

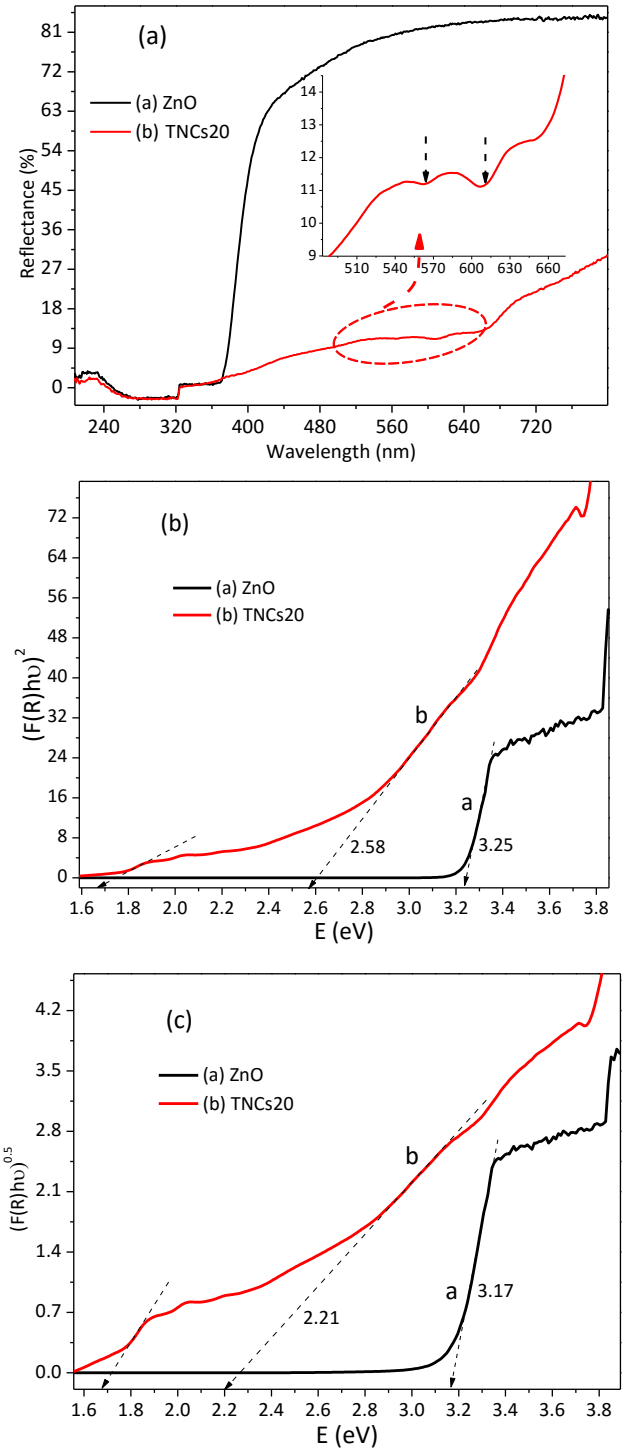

Figure 8. The DRS-UV-vis optical analysis for ZnO and TNCs20. (a) the % reflectance versus wavelength plot, (b) the direct and (c) the indirect Kubelka-Munk functions.

The direct and indirect band gaps for ZnO are 3.25 and 3.17 eV, respectively, whereas the TNCs have 2.58 and 2.21 eV. The decrease in the bandgap (redshift)

for the TNCs is due to the copper and cobalt inclusion, which creates an additional energy level within the ZnO band gap. The indirect band gap, which has different crystal momentum for the minimum conduction band and maximum valance band values, has a novel capacity for producing photon-induced electrons and holes, which are beneficial in different applications such as catalysis (Schneider, 2020).

4.1.5. Fourier transforms-infrared analysis

The band vibration-based metal-oxygen bond properties were characterized using the Fourier transforms—infrared spectroscopic analysis, as shown in Fig. 9a. The characteristic metal oxygen vibrations in the fingerprint region of 400–600 cm^{-1} are attributed to the (Co, Cu, and Zn)-O bending vibration (Demircan et al., 2022). The metal-oxygen bond that was formed, specifically for 20% BNCS and TNCs, as a result of the microstructure change caused by Co/Cu inclusion at 675 cm^{-1}, is not visible on the ZnO (Mesaros et al., 2014). Besides, an intensity change due to the effect of Co/Cu inclusion was also detected at 1370 cm^{-1} (see the magnified image for clarity, Fig. 9b). The disturbed type of band detected at about 2340 cm^{-1} commonly occurs due to CO_2 absorption (Borah et al., 2019). The NPs and NCs spectra have almost similar band positions, except for intensity differences. The bands detected at 3415 cm^{-1}, 1634 cm^{-1}, and 1393 cm^{-1} are due to the O-H stretching and H-O-H bending vibrations of surface or interstitially absorbed H_2O molecules, respectively (Majeed Khan et al., 2020).

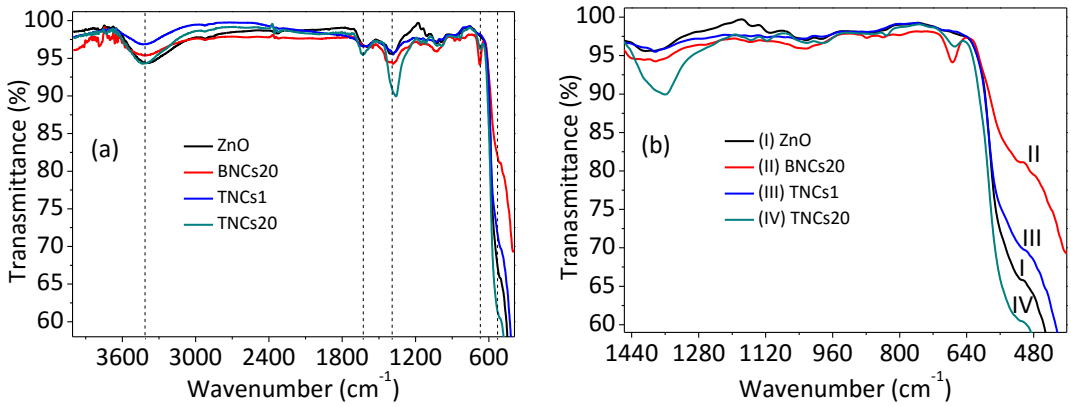

Figure 9. FTIR spectroscopy for chemical bonding study: (a) FTIR spectra of zinc oxide NPs, BNCs, and TNCs. (b) the magnified view of Fig. 9a.

4.1.6. Cyclic voltammetry analysis

The electrochemical property measurements of ZnO NPs and TNCs were characterized by cyclic voltammetry (CV), as shown in Fig. 10. As seen from the ZnO NPs modified electrode cyclic voltammogram, no oxidation-reduction peak was detected (Fig. 10a). However, at different potential values, the TNCs modified electrode cyclic voltammogram revealed two oxidations and two reductions (two pairs of redox) peaks (Fig. 10b), indicating improvements in the conductivity, charge transfer, and catalytic properties of the modified TNCs materials (Wang et al., 2016). The redox peaks on the TNCs are due to the reduction and oxidation reactions of zinc, copper, and cobalt. Furthermore, as the scan rate increased from 10 to 50 mV/s, the potential shift from left to right was observed; this indicates the presence of unrestricted diffusion. This diffusion-type controlled species' unrestricted movement without adsorption on the electrode surface was also confirmed by the well-fitting (R^2 equal to 0.9893) of the potential versus the current plot (see the inset in Fig. 10a) (Haque et al., 2020).

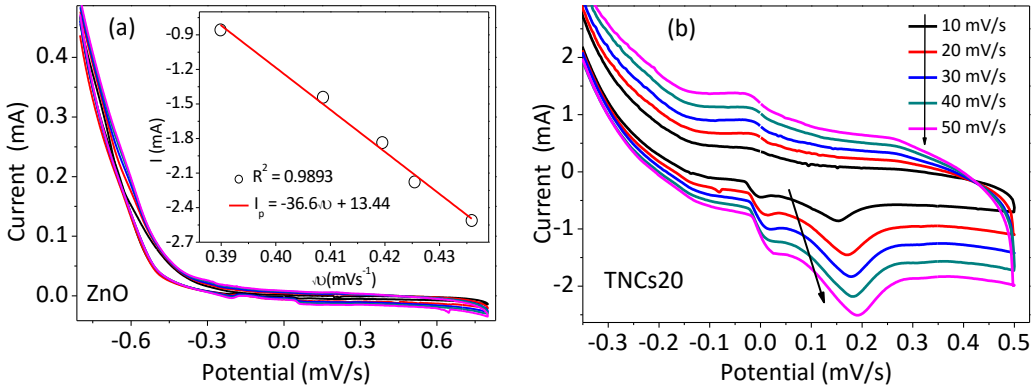

Figure 10. Cyclic voltammetry analysis: (a) A cyclic voltammogram of ZnO NPs (b) A cyclic voltammogram of 20% TNCs, and the inset is the square root versus anodic peak current linear plot of TNCs.

4.1.7. Scanning electron microscopy-energy dispersive X-ray analysis

SEM-EDS and TEM image analyses were used to characterize the morphology of the synthesized materials, as shown in Fig. 11 and 12. The low-scale SEM images of ZnO, BNCs (1% and 10%), and TNCs (1% and 10%) showed the presence of porosity improvements for BNCs and TNCs compared to bare zinc oxide NPs (Fig. 12a). Besides, the TNCs have better porosity than the single ZnO NPs. This higher porosity for TNCs may confirm the copper and cobalt nitrate salts are increasing the combustion process.

Besides, increasing the dopant amount in the TNCs to 20% resulted in the production of more porous materials than ZnO NPs due to the increased gas evolution (Fig. 11a and 11b). The evolution of gases starts at the point of precursor-PVA surfactant complex ignition temperature after the formation of sol and gel (Abebe and Murthy, 2022). The complex ignition may start from one point to give a trade-like product or from many points to give a sponge-type product (Carlos et al., 2020; Nersisyan et al., 2017). A sponge-like morphology was observed in this study, confirming the complex is initiated from multiple points (Abebe et al., 2022). The compositional analysis was performed using the energy dispersive X-ray (EDX) technique, as seen in Fig. 12b. The amounts in percent weight for copper (7.78 wt%) and cobalt (7.77 wt%) are almost proportional to the proposed amounts during synthesis (Fig. 12b inset). Besides, elemental mapping using the EDS analysis also showed the presence of good distributions of copper and cobalt on the ZnO surface, as shown in Fig. 11c. The EDS mapping analysis was conducted from the EDS legend image of the SEM image (Fig. 11d). The representative zinc, oxygen, cobalt, and copper EDS mapping images were also given as red, green, purple, and aqua colors, respectively, as shown in Fig. 11.

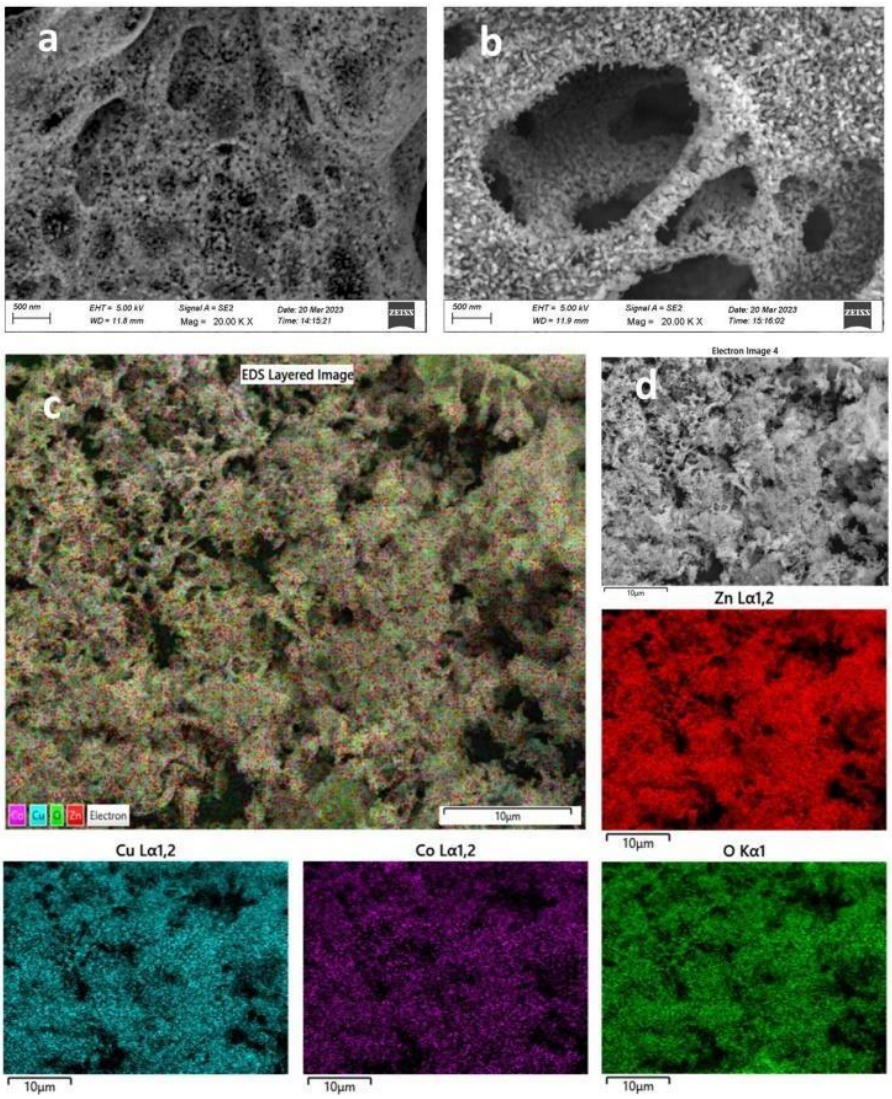

Figure 11. Morphological and compositional analysis using SEM-EDS: (a) and (b) are the SEM images of ZnO NPs and 20% TNCs, respectively. The 20% TNCs showed greater porosity compared to the ZnO NPs. (c) A 20% TNCs EDS-layered image of the SEM image is shown in (d). The red, green, purple, and aqua images are the elemental mapping images for zinc, oxygen, cobalt, and copper, respectively.

(a)

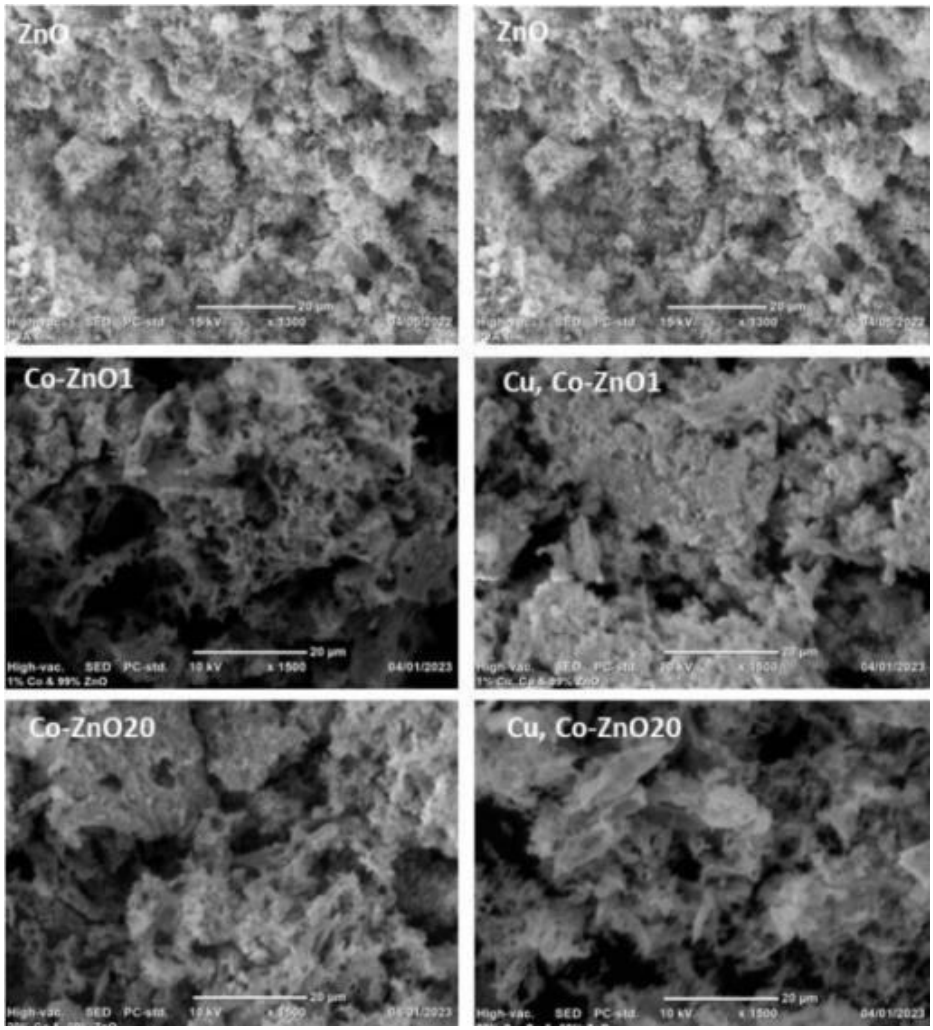

(b)

Figure 12. Image analysis using scanning electron microscopy (SEM): (a) the SEM image of ZnO NPs and 1% and 20% BNCs and TNCs. The nanocomposites showed greater porosity compared to the ZnO NPs. (b) The EDX analysis for the 20% TNCs; the inset table in the EDX image is the detailed compositional analysis.

4.1.8. Morphological analysis

The pore observed due to gas evolution on the NPs and TNCs was also observed on the TEM images (Fig. 13a and 13c). The agglomerated-type morphology for ZnO NPs, compared to the TNCs, is also confirmed on the TEM image. The particle sizes (not crystallite sizes) of the NPs and TNCs were verified to be between 40 and 70 nm. The selected-area electron diffraction (SAED) ring analysis results for ZnO NPs and TNCs are shown in the TEM images as insets (inset Fig. 13a and 13c, respectively). There are several bright spots on the ZnO NPs SAED ring as compared to the NCs, indicating the greater crystallinity of the ZnO NPs. The spots present on the ring are for ZnO crystal, whereas the spots outside of the ring are due to the dopants (Zhai et al., 2012). The d-spacing values deduced from the HRTEM images of NPs and NCs were obtained to be 0.28 nm and 0.13 nm, respectively (Fig. 13b and 13d, respectively). The obtained d-spacing value of 0.28 nm for ZnO NPs matches the (002) crystal plane of hexagonal ZnO NPs. The obtained d-spacing value of 0.13 nm on the NCs is the (-220) crystal plane of CuO NPs (Rawat et al., 2020).

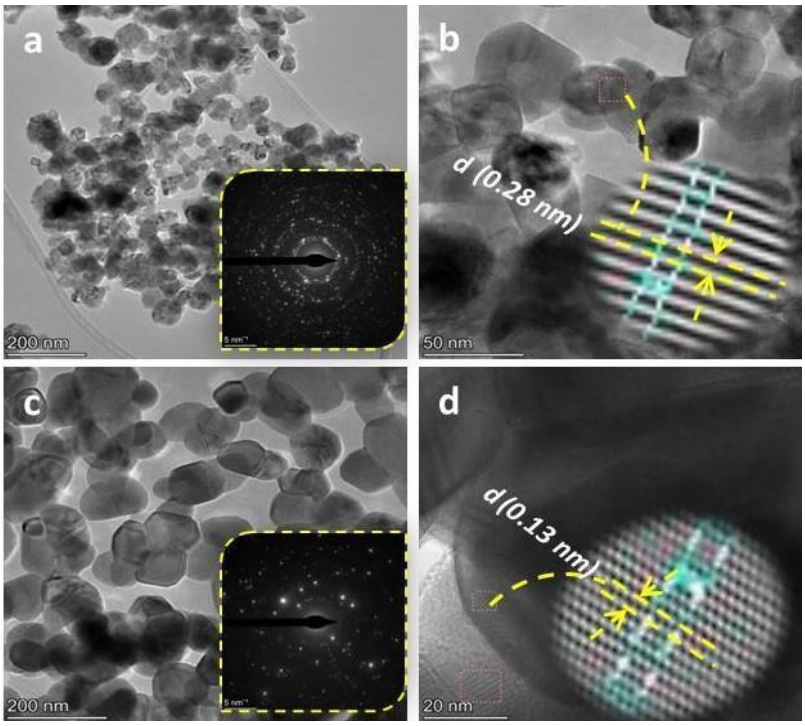

Figure 13. Image analysis using transmission electron microscopy (TEM): ZnO NPs (a and c) and 20% TNCs (b and d) TEM and HRTEM images, respectively. The inset images in Fig. 13a and 13c are the selected-area electron diffraction rings for ZnO and TNCs, respectively. The selected-area electron diffraction inset images in Figure 13a and 13c are the XRD patterns for ZnO and TNCs, respectively.

4.2. 4-Nitrophenol Reduction

The reduction reaction was controlled on the UV-vis spectrometer in the presence and absence of the catalysts. The catalytic reduction of 4-nitrophenol to 4-aminophenol was investigated, as shown in Fig. 14. 4-nitrophenol has a light yellow color in an aqueous solution and a maximum wavelength of 318 nm (Fig. 14a, inset label I). The catalytic reduction process of 4-nitrophenol proceeded in the presence of $NaBH_4$ as a reducing agent. First, the addition of $NaBH_4$ to the 4-nitrophenol aqueous solution forms boron hydride ions. During the addition of the $NaBH_4$, a slight evolution of bubbles due to hydrogen removal was observed. Adding the $NaBH_4$ to the 4-nitrophenol, results in a change of color from a light yellow to a dark yellow due to the formation of 4-nitrophenolate ions. The 4-nitrophenolate ions have a maximum wavelength of 400 nm (Fig. 14a, inset label II). With the addition of the TNCs or ZnO NPs as catalysts, the boron hydride ions adsorb on the surface and form metal hydride complexes.

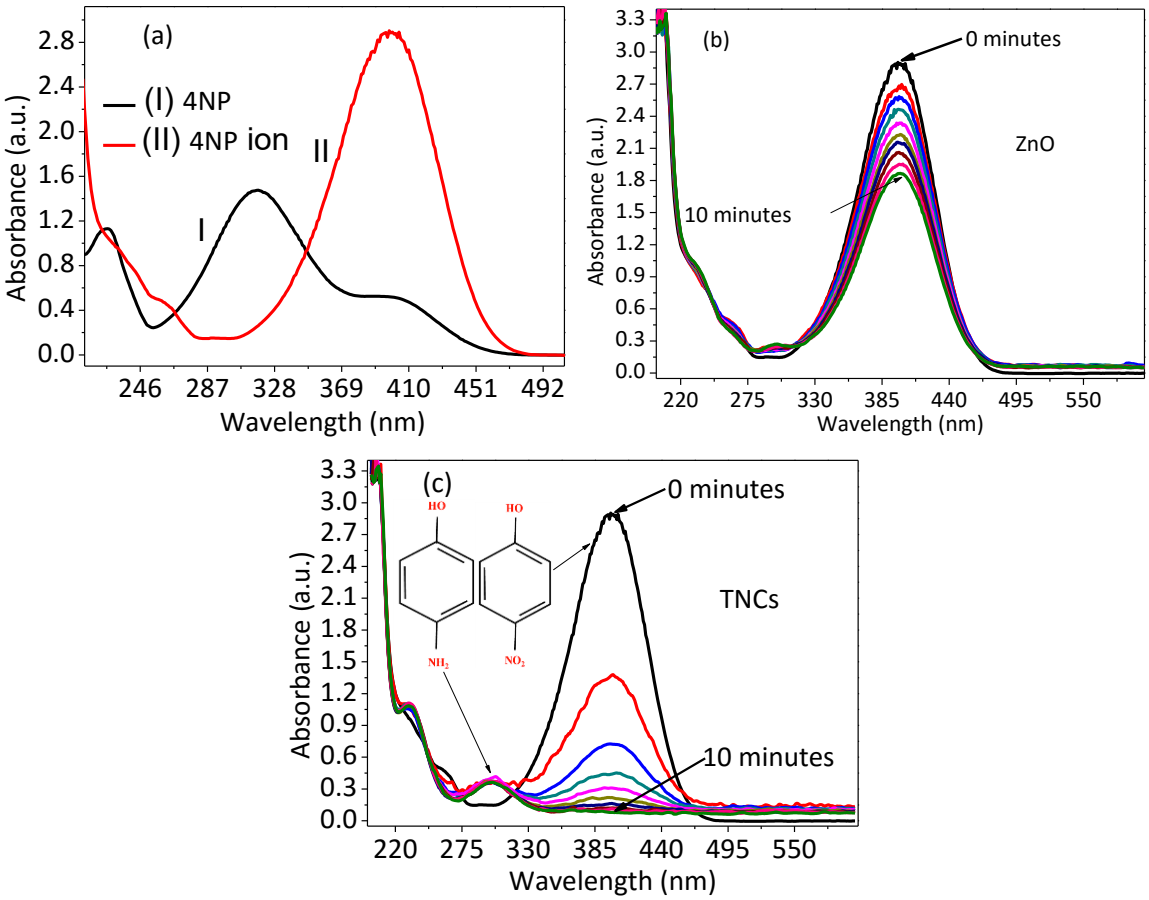

Figure 14. The 4-nitrophenol to 4-aminophenol catalytic reduction reaction: (a) 4-nitrophenol and 4-nitrophenolate ion spectra, (b) ZnO NPs, and (c) TNCs.

With the addition of the catalyst, a larger bubble was formed. Then, the adsorption of 4-nitrophenol on the surface of metal hydride complexes results in the reduction process (Kong et al., 2017; Mejía and Reddy Bogireddy, 2022; Wang et al., 2017). During the catalytic reduction process, the decrease in the 4-nitrophenolate ion peak at 400 nm results in an increase in the 4-aminophenol peak at 300 nm. Of course, the formation of 4-hydroxyl aminophenol as a transition state was reported before the occurrence of 4-aminophenol (Wang et al., 2017). The total catalytic reduction process in the presence of ZnO NPs and TNCs was accomplished within ten minutes. However, the ZnO NPs (Fig. 14b) have slower reduction activity compared to the TNCs (Fig. 14c) (Wang et al., 2017). The slight ZnO catalytic reduction reaction occurred due to the defects generated during combustion (Nadupalli et al., 2021).

4.3. Thiazine Methylene Blue Reduction

The TMB dye redox reaction in the presence of $NaBH_4$ as a reducing agent and NPs and NCs as catalysts was also tested, as shown in Fig. 15. After the addition of the $NaBH_4$ to the TMB dye, a slight color change was observed for about 3–5 minutes. However, no TMB dye catalytic reduction was performed due to $NaBH_4$, as shown in the UV-vis spectra in Fig. 15a. Thus, the observed color change during $NaBH_4$ addition is due to the white color of the $NaBH_4$. After the addition of the catalyst, a color change from blue to colorless was observed. Still, the color change for ZnO NPs was very slow, with only a slight change from blue to light blue (Fig. 15b). However, for the NCs, the complete fading of the blue color to colorless was observed within five minutes (Fig. 15c). The complete disappearance of blue indicates the reduction of TMB to leucomethylene blue (LMB) (Naseer et al., 2022). The greater reduction potential of the NCs than ZnO NPs is due to the presence of greater surface electron transfer resulting from doping or hetero junction. Of course, the catalytic reduction of ZnO NPs is low due to electron-hole recombination, which diminishes the interfacial charge transfer process.

Recent studies (Godiya et al., 2023; Naseer et al., 2022; Taghizadeh and Rad-Moghadam, 2018; Wang et al., 2021) have been used to develop the mechanism of TMB-to-LMB reduction. In detail, during the addition of the catalyst to the pollutant solution in the presence of $NaBH_4$, the catalyst-boron hydride ion bond

formed, and then the pollutant was adsorbed on the catalyst-boron hydride ion surface via π–π stacking interactions. Then, the boron hydride ion becomes bonded with the pollutant. Now then, electrons are continuously transferred from the boron hydride ion to the pollutant, which results in the reduction of TMB to LBM (Wang et al., 2021). Because of the presence of interfacial contact and doping, the charge carrier recombination process in NCs was slowed (Naseer et al., 2022; Taghizadeh and Rad-Moghadam, 2018). With the addition of 3 mL of 0.01 M NaOH solution (the result is not presented), the blue color immediately reappeared. The reappearance of a blue color indicates that the catalyst is acting as a bridge between the borohydride ion and the methylene blue ion for electron transfers instead of degrading the pollutant (Ray et al., 2013).

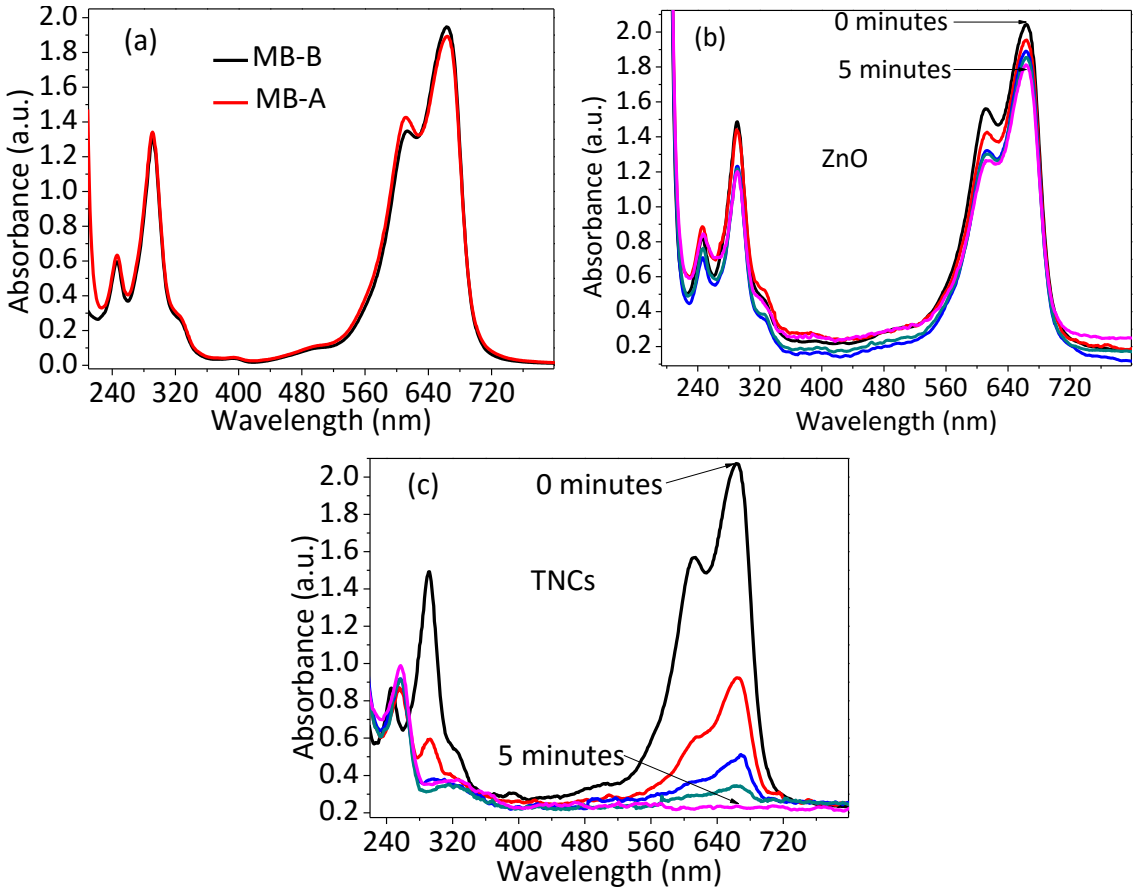

Figure 15. The methylene blue to leucomethylene blue catalytic reduction reaction: methylene blue to leucomethylene blue reduction potential of (a) sodium borohydride, (b) ZnO NPs, and (c) TNCs.

5. Conclusions and Recommendations

5.1. Conclusions

In conclusion, the SG-SC approach is an efficient method for synthesizing doped composites with little time and energy and a less complex procedure. Image analysis by SEM, TEM, and HRTEM confirmed the materials' porosity, nanoscale-sized particles (40–70 nm), and better crystallinity of ZnO NPs. The occurrences of doping and hetero junction within TNCs were verified by X-ray diffraction analysis. The presence of a greater charge transfer process for TNCs than that of single ZnO NPs was verified from the photoluminescence spectroscopic analysis. The greater bandgap reduction for the TNCs from 3.17 to 2.21 eV (the indirect one) was due to the inclusion of copper and cobalt in the ZnO lattice. The formation of a metal-oxygen bond was confirmed using FTIR spectroscopy. The efficient reduction of toxics to less toxic pollutants was demonstrated in the presence of sodium borohydride as a reducing agent. Thus, the SG-SC synthesis approach is effective in synthesizing porous catalyst materials with less energy and time, especially for an industrially accessible catalytic analysis.

5.2. Recommendations

One of the popular methods for improving the photoactivity of semiconductor nanomaterials is semiconductor doping, which does so by boosting photon-capture effectiveness in the visible light spectrum. Many studies, including this one, give presumed proposals on doping inclusion and distribution. When interpreting data, various false assumptions and mistakes are routinely made that can produce erroneous conclusions concerning the impact of doping on catalysis. One of them is figuring out where the dopants are and their distribution. The difference between surface modification and bulk alteration can be difficult to identify. Thus, since the doping chemistry is not easily understandable by techniques such as XRD and SEAM, the authors recommend further studies using advanced techniques such as X-ray absorption spectroscopy (XAS) and Scanning transmission electron microscopy (STEM) with various detectors.

6. References

Abebe, B., Murthy, H.C.A., 2022. Insights into ZnO-based doped porous nanocrystal frameworks. RSC Adv. 12, 5816–5833. https://doi.org/10.1039/D1RA09152B

Abebe, B., Murthy, H.C.A., Amare, E., 2020. Enhancing the photocatalytic efficiency of ZnO: Defects, heterojunction, and optimization. Environ. Nanotechnology, Monit. Manag. 14, 100336. https://doi.org/10.1016/j.enmm.2020.100336

Abebe, B., Tsegaye, D., Ananda Murthy, H.C., 2022. Insight into nanocrystal synthesis: from precursor decomposition to combustion. RSC Adv. 12, 24374–24389. https://doi.org/10.1039/D2RA05222A

Abu Hatab, A.S., Ahmad, Y.H., Abdul Rahman, M.B., Al-Qaradawi, S.Y., 2022. Solution combustion synthesis of Ni-based hybrid metal oxides for oxygen evolution reaction in alkaline medium. RSC Adv. 12, 1694–1703. https://doi.org/10.1039/D1RA07304D

Agarwal, D.C., Singh, U.B., Gupta, S., Singhal, R., Kulriya, P.K., Singh, F., Tripathi, A., Singh, J., Joshi, U.S., Avasthi, D.K., 2019. Enhanced room temperature ferromagnetism and green photoluminescence in Cu doped ZnO thin film synthesised by neutral beam sputtering. Sci. Rep. 9, 6675. https://doi.org/10.1038/s41598-019-43184-9

Ajamein, H., Haghighi, M., 2016. Influence of ambient gas on microwave-assisted combustion synthesis of CuO–ZnO–Al2O3 nanocatalyst used in fuel cell grade hydrogen production via methanol steam reforming. Ceram. Int. 42, 17978–17989. https://doi.org/10.1016/j.ceramint.2016.07.092

Ali, N., Singh, B., Khan, Z.A., A. R., V., Tarafder, K., Ghosh, S., 2019. Origin of ferromagnetism in Cu-doped ZnO. Sci. Rep. 9, 2461. https://doi.org/10.1038/s41598-019-39660-x

Alias, S.S., Ismail, A.B., Mohamad, A.A., 2010. Effect of pH on ZnO nanoparticle properties synthesized by sol–gel centrifugation. J. Alloys Compd. 499, 231–237. https://doi.org/10.1016/j.jallcom.2010.03.174

Bagheri, M., Melillo, A., Ferrer, B., Masoomi, M.Y., Garcia, H., 2022. Quasi-HKUST Prepared via Postsynthetic Defect Engineering for Highly Improved Catalytic Conversion of 4-Nitrophenol. ACS Appl. Mater. Interfaces 14, 978–989. https://doi.org/10.1021/acsami.1c19862

Basu, M., Sinha, A.K., Pradhan, M., Sarkar, S., Pal, A., Mondal, C., Pal, T., 2012. Methylene Blue–Cu 2 O Reaction Made Easy in Acidic Medium. J. Phys. Chem. C 116, 25741–25747. https://doi.org/10.1021/jp308095h

Beltrán, J.J., Osorio, J.A., Barrero, C.A., Hanna, C.B., Punnoose, A., 2013. Magnetic properties of Fe doped, Co doped, and Fe+Co co-doped ZnO. J. Appl. Phys. 113, 17C308. https://doi.org/10.1063/1.4799778

Bhardwaj, R., Bharti, A., Singh, J.P., Chae, K.H., Goyal, N., 2020. Influence of Cu doping on the local electronic and magnetic properties of ZnO nanostructures. Nanoscale

Adv. 2, 4450–4463. https://doi.org/10.1039/D0NA00499E

Borah, M.J., Devi, A., Borah, R., Deka, D., 2019. Synthesis and application of Co doped ZnO as heterogeneous nanocatalyst for biodiesel production from non-edible oil. Renew. Energy 133, 512–519. https://doi.org/10.1016/j.renene.2018.10.069

Cai, B., Liu, H., Han, W., 2020. Solution Combustion Synthesis of Fe2O3-Based Catalyst for Ammonia Synthesis. Catalysts 10, 1027. https://doi.org/10.3390/catal10091027

Cao, L., Wang, L., Xu, L., Shen, Y., Xie, M., Hao, H., 2021. Controllable growth of Cu–Bi co-doped ZnO nanospheres on cotton fabrics and a study on their photocatalytic performance in visible light. RSC Adv. 11, 29416–29425. https://doi.org/10.1039/D1RA05317E

Carlos, E., Martins, R., Fortunato, E., Branquinho, R., 2020. Solution Combustion Synthesis: Towards a Sustainable Approach for Metal Oxides. Chem. – A Eur. J. 26, 9099–9125. https://doi.org/10.1002/chem.202000678

Chang, Y.-C., Lin, P.-S., Liu, F.-K., Guo, J.-Y., Chen, C.-M., 2016. One-step and single source synthesis of Cu-doped ZnO nanowires on flexible brass foil for highly efficient field emission and photocatalytic applications. J. Alloys Compd. 688, 242–251. https://doi.org/10.1016/j.jallcom.2016.07.193

Chen, Z., Fang, Y., Wang, L., Chen, X., Lin, W., Wang, X., 2021. Remarkable oxygen evolution by Co-doped ZnO nanorods and visible light. Appl. Catal. B Environ. 296, 120369. https://doi.org/10.1016/j.apcatb.2021.120369

Chithira, P.R., Theresa John, T., 2020. Correlation among oxygen vacancy and doping concentration in controlling the properties of cobalt doped ZnO nanoparticles. J. Magn. Magn. Mater. 496, 165928. https://doi.org/10.1016/j.jmmm.2019.165928

Chomean, S., Ingkananth, S., Kiatchaipar, M., Kaset, C., 2017. Visible Light Sensitive Mesoporous Cu-Substituted ZnO Nanoassembly for Enhanced Photocatalysis, Bacterial Inhibition, and Noninvasive Tumor Regression. Anal. Chim. Acta 1180, 338884. https://doi.org/10.1021/acssuschemeng.7b01433

Costas, A., Florica, C., Preda, N., Besleaga, C., Kuncser, A., Enculescu, I., 2022. Self-connected CuO–ZnO radial core–shell heterojunction nanowire arrays grown on interdigitated electrodes for visible-light photodetectors. Sci. Rep. 12, 6834. https://doi.org/10.1038/s41598-022-10879-5

de Godoy, M.P.F., Gratens, X., Chitta, V.A., Mesquita, A., de Lima, M.M., Cantarero, A., Rahman, G., Morbec, J.M., de Carvalho, H.B., 2021. Defect induced room temperature ferromagnetism in high quality Co-doped ZnO bulk samples. J. Alloys Compd. 859, 157772. https://doi.org/10.1016/j.jallcom.2020.157772

Deganello, F., Tyagi, A.K., 2018. Solution combustion synthesis, energy and environment: Best parameters for better materials. Prog. Cryst. Growth Charact. Mater. 64, 23–61. https://doi.org/10.1016/j.pcrysgrow.2018.03.001

Delfani, E., Khodabakhshi, A., Habibzadeh, S., Naji, L., Ganjali, M.R., 2022. Novel mesoporous Co 3 O 4 –Sb 2 O 3 –SnO 2 active material in high-performance

capacitive deionization. RSC Adv. 12, 907–920. https://doi.org/10.1039/D1RA07557H

Demircan, G., Yalcin, S., Alivi, K., Ceyhan, G., Acikgoz, A., Balak, M.V., Aktas, B., Das, R., 2022. The effect of Co and Mn Co-Doping on structural and optical properties of ZnO thin films. Opt. Mater. (Amst). 126, 112163. https://doi.org/10.1016/j.optmat.2022.112163

Fan, Y., Xu, Y., Wang, Y., Sun, Y., 2021. Fabrication and characterization of Co-doped ZnO nanodiscs for selective TEA sensor applications with high response, high selectivity and ppb-level detection limit. J. Alloys Compd. 876, 160170. https://doi.org/10.1016/j.jallcom.2021.160170

Gao, Y., Meng, F., Li, X., Wen, J.Z., Li, Z., 2016. Factors controlling nanosized Ni–Al 2 O 3 catalysts synthesized by solution combustion for slurry-phase CO methanation: the ratio of reducing valences to oxidizing valences in redox systems. Catal. Sci. Technol. 6, 7800–7811. https://doi.org/10.1039/C6CY01603K

Godiya, C.B., Kumar, S., Park, B.J., 2023. Superior catalytic reduction of methylene blue and 4-nitrophenol by copper nanoparticles-templated chitosan nanocatalyst. Carbohydr. Polym. Technol. Appl. 5, 100267. https://doi.org/10.1016/j.carpta.2022.100267

González-Cortés, S.L., Imbert, F.E., 2013. Fundamentals, properties and applications of solid catalysts prepared by solution combustion synthesis (SCS). Appl. Catal. A Gen. 452, 117–131. https://doi.org/10.1016/j.apcata.2012.11.024

Gupta, R., KrishnaRao Eswar, N., Modak, J.M., Madras, G., 2016. Visible light driven efficient N and Cu co-doped ZnO for photoinactivation of Escherichia coli. RSC Adv. 6, 85675–85687. https://doi.org/10.1039/C6RA16739J

GuruSampath Kumar, A., Li, X., Du, Y., Geng, Y., Hong, X., 2020. UV-photodetector based on heterostructured ZnO/(Ga,Ag)-co-doped ZnO nanorods by cost-effective two-step process. Appl. Surf. Sci. 509, 144770. https://doi.org/10.1016/j.apsusc.2019.144770

Haque, M., Fouad, H., Seo, H.-K., Othman, A.Y., Kulkarni, A., Ansari, Z.A., 2020. Investigation of Mn Doped ZnO Nanoparticles Towards Ascertaining Myocardial Infarction Through an Electrochemical Detection of Myoglobin. IEEE Access 8, 164678–164692. https://doi.org/10.1109/ACCESS.2020.3021458

Islah-u-din, Salam, W.T., Gillani, S.S.A., Tahir, M.B., Ikram, M., Ali, S., 2020. Tuning the structure and optical properties of nanostructured CdS by Cu doping. Optik (Stuttg). 203, 163966. https://doi.org/10.1016/j.ijleo.2019.163966

Kazmi, J., Ooi, P.C., Raza, S.R.A., Goh, B.T., Karim, S.S.A., Samat, M.H., Lee, M.K., Mohd. Razip Wee, M.F., Taib, M.F.M., Mohamed, M.A., 2021. Appealing stable room-temperature ferromagnetism by well-aligned 1D Co-doped zinc oxide nanowires. J. Alloys Compd. 872, 159741. https://doi.org/10.1016/j.jallcom.2021.159741

Kong, X., Zhu, H., Chen, C., Huang, G., Chen, Q., 2017. Insights into the reduction of 4-

nitrophenol to 4-aminophenol on catalysts. Chem. Phys. Lett. 684, 148–152. https://doi.org/10.1016/j.cplett.2017.06.049

Kumar, S., Krishnakumar, B., Sobral, A.J.F.N., Koh, J., 2019. Bio-based (chitosan / PVA / ZnO) nanocomposites fi lm : Thermally stable and photoluminescence material for removal of organic dye. Carbohydr. Polym. 205, 559–564. https://doi.org/10.1016/j.carbpol.2018.10.108

Lemine, O.M., Almusidi, T., Kanoun, M.B., Goumri-Said, S., Alshammari, M., Abdel All, N., Alanzi, A.Z., Alghamdi, F.S., Alyamani, A., 2019. Room temperature ferromagnetism in ball milled Cu-doped ZnO nanocrystallines: an experimental and first-principles DFT studies. J. Mater. Sci. Mater. Electron. 30, 19833–19840. https://doi.org/10.1007/s10854-019-02350-5

Li, F., Ran, J., Jaroniec, M., Qiao, S.Z., 2015. Solution combustion synthesis of metal oxide nanomaterials for energy storage and conversion. Nanoscale 7, 17590–17610. https://doi.org/10.1039/C5NR05299H

Li, Y., Fu, Z.-Y., Su, B.-L., 2012. Hierarchically Structured Porous Materials for Energy Conversion and Storage. Adv. Funct. Mater. 22, 4634–4667. https://doi.org/10.1002/adfm.201200591

Liu, B., You, Y., Zhang, H., Wu, H., Jin, J., Liu, H., 2016. Synthesis of ZnO nano-powders via a novel PVA-assisted freeze-drying process. RSC Adv. 6, 110349–110355. https://doi.org/10.1039/C6RA24154A

Liu, H., Wang, Y., Wu, J., Zhang, G., Yan, Y., 2015. Oxygen vacancy assisted multiferroic property of Cu doped ZnO films. Phys. Chem. Chem. Phys. 17, 9098–9105. https://doi.org/10.1039/C5CP00086F

Liu, H., Zeng, F., Gao, S., Wang, G., Song, C., Pan, F., 2013. Contributions of magnetic properties in epitaxial copper-doped ZnO. Phys. Chem. Chem. Phys. 15, 13153–13161. https://doi.org/10.1039/c3cp51894a

Luo, X., Tseng, L.T., Lee, W.T., Tan, T.T., Bao, N.N., Liu, R., Ding, J., Li, S., Lauter, V., Yi, J.B., 2017. Probing the magnetic profile of diluted magnetic semiconductors using polarized neutron reflectivity. Sci. Rep. 7, 6341. https://doi.org/10.1038/s41598-017-06793-w

Ma, Y., Choi, T.-W., Cheung, S.H., Cheng, Y., Xu, X., Xie, Y.-M., Li, H.-W., Li, M., Luo, H., Zhang, W., So, S.K., Chen, S., Tsang, S.-W., 2019. Charge transfer-induced photoluminescence in ZnO nanoparticles. Nanoscale 11, 8736–8743. https://doi.org/10.1039/C9NR02020A

Mahmoud, A., Echabaane, M., Omri, K., Boudon, J., Saviot, L., Millot, N., Chaabane, R.B.R. Ben, 2021. Cu-doped ZnO nanoparticles for non-enzymatic glucose sensing. Molecules 26, 929. https://doi.org/10.3390/molecules26040929

Majeed Khan, M.A., Siwach, R., Kumar, S., Ahmed, M., Ahmed, J., 2020. Investigations on microstructure, optical, magnetic, photocatalytic, and dielectric behaviours of pure and Co-doped ZnO NPs. J. Mater. Sci. Mater. Electron. 31, 6360–6371. https://doi.org/10.1007/s10854-020-03192-2

Manjari, G., Saran, S., Radhakrishanan, S., Rameshkumar, P., Pandikumar, A., Devipriya, S.P., 2020. Facile green synthesis of Ag–Cu decorated ZnO nanocomposite for effective removal of toxic organic compounds and an efficient detection of nitrite ions. J. Environ. Manage. 262, 110282. https://doi.org/10.1016/j.jenvman.2020.110282

Mejía, Y.R., Reddy Bogireddy, N.K., 2022. Reduction of 4-nitrophenol using green-fabricated metal nanoparticles. RSC Adv. 12, 18661–18675. https://doi.org/10.1039/D2RA02663E

Mesaros, A., Ghitulica, C.D., Popa, M., Mereu, R., Popa, A., Petrisor, T., Gabor, M., Cadis, A.I., Vasile, B.S., 2014. Synthesis, structural and morphological characteristics, magnetic and optical properties of Co doped ZnO nanoparticles. Ceram. Int. 40, 2835–2846. https://doi.org/10.1016/j.ceramint.2013.10.030

Morales-Mendoza, J.E., Paraguay-Delgado, F., 2021. Widening UV–Vis absorption band by Cu doped ZnO and ZnO/CuO composite. Mater. Lett. 291, 129494. https://doi.org/10.1016/j.matlet.2021.129494

Morris, J.D., Daood, S.S., Chilton, S., Nimmo, W., 2018. Mechanisms and mitigation of agglomeration during fluidized bed combustion of biomass: A review. Fuel 230, 452–473. https://doi.org/10.1016/j.fuel.2018.04.098

Mukasyan, A.S., Rogachev, A.S., Aruna, S.T., 2015. Combustion synthesis in nanostructured reactive systems. Adv. Powder Technol. 26, 954–976. https://doi.org/10.1016/j.apt.2015.03.013

Muthukumaran, S., Gopalakrishnan, R., 2012. Structural, FTIR and photoluminescence studies of Cu doped ZnO nanopowders by co-precipitation method. Opt. Mater. (Amst). 34, 1946–1953. https://doi.org/10.1016/j.optmat.2012.06.004

Nadupalli, S., Repp, S., Weber, S., Erdem, E., 2021. About defect phenomena in ZnO nanocrystals. Nanoscale 13, 9160–9171. https://doi.org/10.1039/D1NR00943E

Nagaveni, K., Sivalingam, G., Hegde, M.., Madras, G., 2004. Solar photocatalytic degradation of dyes: high activity of combustion synthesized nano TiO2. Appl. Catal. B Environ. 48, 83–93. https://doi.org/10.1016/j.apcatb.2003.09.013

Naseer, S., Aamir, M., Mirza, M.A., Jabeen, U., Tahir, R., Malghani, M.N.K., Wali, Q., 2022. Synthesis of Ni–Ag–ZnO solid solution nanoparticles for photoreduction and antimicrobial applications. RSC Adv. 12, 7661–7670. https://doi.org/10.1039/D2RA00717G

Nersisyan, H.H., Lee, J.H., Ding, J.-R., Kim, K.-S., Manukyan, K. V., Mukasyan, A.S., 2017. Combustion synthesis of zero-, one-, two- and three-dimensional nanostructures: Current trends and future perspectives. Prog. Energy Combust. Sci. 63, 79–118. https://doi.org/10.1016/j.pecs.2017.07.002

Novitskaya, E., Kelly, J.P., Bhaduri, S., Graeve, O.A., 2021. A review of solution combustion synthesis: an analysis of parameters controlling powder characteristics. Int. Mater. Rev. 66, 188–214. https://doi.org/10.1080/09506608.2020.1765603

Paraguay-Delgado, F., Hermida-Montero, L.A., Morales-Mendoza, J.E., Durán-Barradas, Z., Mtz-Enriquez, A.I., Pariona, N., 2022. Photocatalytic properties of Cu-containing ZnO nanoparticles and their antifungal activity against agriculture-pathogenic fungus. RSC Adv. 12, 9898–9908. https://doi.org/10.1039/D2RA00863G

Pashchanka, M., Hoffmann, R.C., Gurlo, A., Swarbrick, J.C., Khanderi, J., Engstler, J., Issanin, A., Schneider, J.J., 2011. A molecular approach to Cu doped ZnO nanorods with tunable dopant content. Dalt. Trans. 40, 4307. https://doi.org/10.1039/c0dt01567a

Pragna, E., Ramanadha, M., Sudharani, A., Kumar, K.S., 2021. Nano Synthesis and Characterization of Co and Mn Co-doped ZnO by Solution Combustion Technique. J. Supercond. Nov. Magn. 34, 1507–1516. https://doi.org/10.1007/s10948-021-05874-2

Priya, R., Sahay, P., Saxena, N., Rajput, P., Chawla, V., Sharma, R., Sinha, O.P., Krishna, R., 2021. Systematic study of Ni, Cu co-doped ZnO nanoparticles for UV photodetector application. J. Mater. Sci. Mater. Electron. 32, 2011–2025. https://doi.org/10.1007/s10854-020-04968-2

Rahmanian, R., Mozaffari, S.A., Abedi, M., 2015. Disposable urea biosensor based on nanoporous ZnO film fabricated from omissible polymeric substrate. Mater. Sci. Eng. C 57, 387–396. https://doi.org/10.1016/j.msec.2015.08.004

Rajeshwar, K., de Tacconi, N.R., 2009. Solution combustion synthesis of oxide semiconductors for solar energy conversion and environmental remediation. Chem. Soc. Rev. 38, 1984. https://doi.org/10.1039/b811238j

Rawat, R., Tiwari, A., Arun, N., Rao, S.V.S.N., Pathak, A.P., Rao, S.V., Tripathi, A., 2020. Synthesis of CuO hollow nanoparticles using laser ablation: effect of fluence and solvents. Appl. Phys. A 126, 226. https://doi.org/10.1007/s00339-020-3403-1

Ray, C., Dutta, S., Sarkar, S., Sahoo, R., Roy, A., Pal, T., 2013. A facile synthesis of 1D nano structured selenium and Au decorated nano selenium: Catalysts for the clock reaction. RSC Adv. 3, 24313. https://doi.org/10.1039/c3ra44102d

Ren, Y., Ma, Z., Bruce, P.G., 2012. Ordered mesoporous metal oxides: synthesis and applications. Chem. Soc. Rev. 41, 4909. https://doi.org/10.1039/c2cs35086f

Rossell, M.D., Ramasse, Q.M., Findlay, S.D., Rechberger, F., Erni, R., Niederberger, M., 2012. Direct Imaging of Dopant Clustering in Metal–Oxide Nanoparticles. ACS Nano 6, 7077–7083. https://doi.org/10.1021/nn3021212

Schneider, K., 2020. Optical properties and electronic structure of V2O5, V2O3 and VO2. J. Mater. Sci. Mater. Electron. 31, 10478–10488. https://doi.org/10.1007/s10854-020-03596-0

Shunmuga Sundaram, P., Sangeetha, T., Rajakarthihan, S., Vijayalaksmi, R., Elangovan, A., Arivazhagan, G., 2020. XRD structural studies on cobalt doped zinc oxide nanoparticles synthesized by coprecipitation method: Williamson-Hall and size-strain plot approaches. Phys. B Condens. Matter 595, 412342. https://doi.org/10.1016/j.physb.2020.412342

Singh, P., Kumar, R., Singh, R.K., 2019. Progress on Transition Metal-Doped ZnO Nanoparticles and Its Application. Ind. Eng. Chem. Res. 58, 17130–17163. https://doi.org/10.1021/acs.iecr.9b01561

Subash, B., Krishnakumar, B., Velmurugan, R., Swaminathan, M., Shanthi, M., 2012. Synthesis of Ce co-doped Ag–ZnO photocatalyst with excellent performance for NBB dye degradation under natural sunlight illumination. Catal. Sci. Technol. 2, 2319. https://doi.org/10.1039/c2cy20254a

Taghizadeh, A., Rad-Moghadam, K., 2018. Green fabrication of Cu/pistachio shell nanocomposite using Pistacia Vera L. hull: An efficient catalyst for expedient reduction of 4-nitrophenol and organic dyes. J. Clean. Prod. 198, 1105–1119. https://doi.org/10.1016/j.jclepro.2018.07.042

Thakur, S., Mandal, S.K., 2021. Investigating the formation of diverse ZnO nanostructures based on solvent, temperature, and pH as adjustable parameters. Mater. Adv. 2, 511–524. https://doi.org/10.1039/D0MA00781A

Thangasamy, P., Selvakumar, K., Sathish, M., Kumar, S.M.S., Thangamuthu, R., 2017. Anchoring of ultrafine Co 3 O 4 nanoparticles on MWCNTs using supercritical fluid processing and its performance evaluation towards electrocatalytic oxygen reduction reaction. Catal. Sci. Technol. 7, 1227–1234. https://doi.org/10.1039/C6CY02611G

Wang, G., Zhao, K., Gao, C., Wang, J., Mei, Y., Zheng, X., Zhu, P., 2021. Green synthesis of copper nanoparticles using green coffee bean and their applications for efficient reduction of organic dyes. J. Environ. Chem. Eng. 9, 105331. https://doi.org/10.1016/j.jece.2021.105331

Wang, L.-Y., Wang, M.-Q., Yao, C.-B., Yin, H.-T., Liu, X.-J., Shi, B.-Y., 2022. Two-step strategy, growth mechanism and optical properties of plasmonic Ag-modified ZnO nanomaterials. RSC Adv. 12, 3013–3026. https://doi.org/10.1039/D1RA09457B

Wang, Z., Su, R., Wang, D., Shi, J., Wang, J.-X., Pu, Y., Chen, J.-F., 2017. Sulfurized Graphene as Efficient Metal-Free Catalysts for Reduction of 4-Nitrophenol to 4-Aminophenol. Ind. Eng. Chem. Res. 56, 13610–13617. https://doi.org/10.1021/acs.iecr.7b03217

Wang, Z., Tian, Z., Han, D., Gu, F., 2016. Highly Sensitive and Selective Ethanol Sensor Fabricated with In-Doped 3DOM ZnO. ACS Appl. Mater. Interfaces 8, 5466–5474. https://doi.org/10.1021/acsami.6b00339

Xanthopoulou, G., Thoda, O., Roslyakov, S., Steinman, A., Kovalev, D., Levashov, E., Vekinis, G., Sytschev, A., Chroneos, A., 2018. Solution combustion synthesis of nano-catalysts with a hierarchical structure. J. Catal. 364, 112–124. https://doi.org/10.1016/j.jcat.2018.04.003

Xu, C., Yang, K., Huang, L., Wang, H., 2009. Cu-doping induced ferromagnetism in ZnO nanowires. J. Chem. Phys. 130, 124711. https://doi.org/10.1063/1.3100505

Xu, D.H., Shen, W.Z., 2012. Cu-Doped ZnO Hemispherical Shell Structures: Synthesis and Room-Temperature Ferromagnetism Properties. J. Phys. Chem. C 116, 13368–13373. https://doi.org/10.1021/jp3003849

Zhai, T., Xie, S., Zhao, Y., Sun, X., Lu, X., Yu, M., Xu, M., Xiao, F., Tong, Y., 2012. Controllable synthesis of hierarchical ZnO nanodisks for highly photocatalytic activity. CrystEngComm 14, 1850. https://doi.org/10.1039/c1ce06013a

Zhang, J., Guo, Q., Liu, Y., Cheng, Y., 2012. Preparation and Characterization of Fe 2 O 3 /Al 2 O 3 Using the Solution Combustion Approach for Chemical Looping Combustion. Ind. Eng. Chem. Res. 51, 12773–12781. https://doi.org/10.1021/ie301804c

Zhang, J., Tse, K., Wong, M., Zhang, Y., Zhu, J., 2016. A brief review of co-doping. Front. Phys. 11, 117405. https://doi.org/10.1007/s11467-016-0577-2